The Lockman-SpReSo Project. Spectroscopic Analysis of Type 1 Active Galactic Nuclei

Castalia Alenka Negrete[1] , Héctor J. Ibarra-Medel[2] , Erika Benítez[2] , Irene Cruz-González[2] , Yair Krongold[2] ,
J. Jesús González[2], Jordi Cepa[3,4] , Carmen Padilla-Torres[3,4,5], Miguel Cerviño[6], Mirjana Povic[7,8,9],
Martín Herrera-Endoqui[2], Nancy Jenaro-Ballesteros[2], Takamitsu Miyaji[10] , Mauricio Elías-Chávez[10],
Miguel Sánchez-Portal[11], Bernabé Cedrés[3], Jakub Nadolny[3,12] , Mauro González-Otero[13], Bereket Assefa[8,14],
Héctor Hernández-Toledo[2], J. Antonio de Diego[2] , J. Ignacio González-Serrano[15], and A. M. Pérez-García[13,16]

[1] SECIHTI Researcher - Instituto de Astronomía, Universidad Nacional Autónoma de México, A.P. 70-264, Ciudad de México, CDMX 04510, México;
alenka@astro.unam.mx
[2] Instituto de Astronomía, Universidad Nacional Autónoma de México, A.P. 70-264, Ciudad de México, CDMX 04510, México
[3] Instituto de Astrofísica de Canarias, E-38205 La Laguna, Tenerife, Spain
[4] Departamento de Astrofísica, Universidad de La Laguna (ULL), E-38205 La Laguna, Tenerife, Spain
[5] Fundación Galileo Galilei—INAF, Rambla José Ana Fernández Pérez, 7, 38712 Breña Baja, TF, Spain
[6] Centro de Astrobiología (CAB, CSIC-INTA), 28692 ESAC Campus, Villanueva de la Cañada, Madrid, Spain
[7] Instituto de Astrofísica de Andalucía (CSIC), 18080 Granada, Spain
[8] Space Science and Geospatial Institute (SSGI), Entoto Observatory and Research Center (EORC), Astronomy and Astrophysics Research Division, PO Box 33679,
Addis Abbaba, Ethiopia
[9] Physics Department, Mbarara University of Science and Technology (MUST), Mbarara, Uganda
[10] Instituto de Astronomía -Ensenada, Universidad Nacional Autónoma de México, Km. 107 Carret. Tijuana-Ensenada, Ensenada 22860, México
[11] Institut de Radioastronomie Millimétrique, Avenida Divina Pastora, 7, Local 20, E 18012 Granada, Spain
[12] Astronomical Observatory Institute, Faculty of Physics and Astronomy, Adam Mickiewicz University, ul. Sloneczna 36, 60-286 Poznań, Poland
[13] Asociación Astrofísica para la Promoción de la Investigación, Instrumentación y su Desarrollo, ASPID, 38205 La Laguna, Tenerife, Spain
[14] Debre Berhan University, Debre Berhan, Ethiopia
[15] Dpto. de Física Moderna, Universidad de Cantabria, IFCA, 39005 Santander, Spain
[16] Centro de Astrobiología (CSIC/INTA), 28692 ESAC Campus, Villanueva de la Cañada, Madrid, Spain

Abstract

We present the first optical-UV spectral systematic analysis of 30 Type 1 active galactic nuclei selected in the far-infrared and X-ray in the Lockman-SpReSO Survey. The sample of faint objects ($m_B = 19.6–21.8$) covers a large redshift range of $0.33 > z > 4.97$ with a high signal-to-noise ratio (~ 21 on average). A detailed spectral analysis based on the quasar main-sequence phenomenology prescription was applied to deblend the principal optical-UV emitting regions. Our sample spans a bolometric luminosity range of $44.85 < \log L_{bol} < 47.87$, absolute B-magnitude of $20.46 > M_B > -26.14$, BH mass of $7.59 < \log M_{BH} < 9.80$, and Eddington ratio of $-1.70 < \log R_{Edd} < 0.56$. The analysis shows that 18 high-z objects correspond to Population (Pop) B, whereas three low-z fall in Pop A2, B1, and B1+. The remaining eight are candidates to be Pop B and one Pop A object. None of them is an extreme accretor. We looked for tendencies in our sample and compared them with other samples with different selection criteria. Evidence for winds was explored using the C IV λ1549 line half-height centroid $c_{(1/2)}$, finding wind velocities between 941 and -1587 km s^{-1}. This result is consistent with samples with similar ranges of z and M_B. The Baldwin effect showed a slope of -0.23 ± 0.03 dex consistent with previous studies. Spectra from 12 objects in our sample were found in the Sloan Digital Sky Survey Data Release 17 database. We applied the same methodology to compare them to our spectra, finding no evidence of variability.

Unified Astronomy Thesaurus concepts: Active galaxies (17); Quasars (1319); Optical astronomy (1776); Surveys (1671)

Materials only available in the online version of record: figure set

1. Introduction

Extragalactic surveys are fundamental building blocks for studying galaxy evolution using data over a wide range of wavelengths. One of the deep fields largely studied is the Lockman Hole (LH). The LH is the best Galactic window, well known for having small amounts of neutral hydrogen column density (N_H). Its central region has a hydrogen column density of $N_H = 5.8 \times 10^{19}$ cm^{-2} (F. J. Lockman et al. 1986; J. M. Dickey & F. J. Lockman 1990), and has been studied with a wide wavelength coverage (e.g., S. Fotopoulou et al.

2012; R. Kondapally et al. 2021; M. Gonzalez-Otero et al. 2023, hereafter GO23), making it an ideal region for cosmological studies, particularly in the infrared (IR).

The Lockman Spectroscopic Redshift Survey using Optical System for Imaging and low-Intermediate-Resolution Integrated Spectroscopy (OSIRIS) at the Gran Telescopio Canarias (GTC; Lockman-SpReSO (LS); GO23) is a large guaranteed time program that provides deep optical spectroscopy of the far-infrared (FIR) sources from the Herschel-PEP survey observed at 100 and 160 μm (D. Lutz et al. 2011), having optical counterparts in images from OSIRIS in the Sloan Digital Sky Survey (SDSS) r band.

This survey is intended to complement previous data obtained by space telescopes such as XMM-Newton, Spitzer, and Herschel, as well as radio data. The LS Survey provided a

total of 1144 sources in the central $24' \times 24'$ region of the LH for a limiting magnitude of $R_C \leqslant 24.5$ (see Figure 2; GO23); of these, 107 are stellar, and 1037 are extragalactic sources. Details of the characterization of the LS objects are presented in GO23. In particular, the LS Survey aims to establish the principal properties of active and star-forming galaxies in this field and identify new sources using the obtained spectral data.

Within the extragalactic sources, 114 galaxies with nuclear activity have been identified. To achieve a comprehensive study on active galactic nuclei (AGNs), it is important to consider the effects of extinction in the spectra when performing those studies. While a dust extinction correction can be applied, it is always assumed based on a dust model. Therefore, it is important to look for places in the galaxy where the transparency is high enough to allow us to obtain observations where the extinction is minimal. In that sense, the LH is the perfect location to perform and study different types of AGNs.

For more than three decades, there have been considerable efforts to organize quasars[17] based on their observable properties at different wavelengths (e.g., T. A. Boroson & R. F. Green 1992; J. W. Sulentic et al. 2000b; Y. Shen & L. C. Ho 2014). The so-called "quasar main sequence" (QMS; see S. Panda 2024, for a recent review) has evolved from the four-dimensional Eigenvector 1, which comprises optical data, including measurements of virialized components of the central region: the FWHM of the Hβ broad component (Hβ_{BC}) and $R_{Fe\,II}$, the ratio of equivalent widths (EW) of Fe II (computed in the wavelength range from 4435 to 4685 Å) and Hβ_{BC}; data in the UV considering the centroid at half intensity $c_{(1/2)}$ of C IVλ1549 as a measure of the contribution of the nonvirialized component due to outflows; and the soft X-ray spectral index as a measure of the contribution of ionizing photons that illuminates the broad-line region (BLR). Type 1 AGNs have been successfully characterized with the QMS formalism, including high-z objects, as was found recently using James Webb Space Telescope observations (e.g., F. Loiacono et al. 2024). The QMS finds a dichotomy of Type 1 AGNs, dividing them into Pop A and Pop B using the FWHM(Hβ) = 4000 km s^{-1} as a boundary. For instance, evidence supporting this division is the change of the Hβ profile from Lorentzian (more adequate to fit Pop A emission line profiles) to double Gaussian, with a redward asymmetry for Pop B objects (see P. Marziani et al. 2018).

This work aims to characterize the Type 1 AGN found in the LS survey based on the QMS formalism, and to analyze their properties with other quasar samples at high and low redshifts. A previous study with observations from almost three decades ago reported 43 quasar spectra in the LH (I. Lehmann et al. 2000, see also D. P. Schneider et al. 1998 for a single quasar at $z = 4.45$). Other previous works in the optical range of AGNs in the LH field have focused on its photometric properties (e.g., E. Rovilos et al. 2011).

In addition, studies using AGNs in the LS project will be addressed in different papers. For instance, the results obtained from the Type 2 AGN sample will be presented in B. Assefa et al. (2025, in preparation) along with new identifications of Compton-thick AGNs. A multicomponent spectral energy distribution analysis using CIGALE (M. Boquien et al. 2019) will be presented in M. Herrera-Endoqui et al. (2025, in

---

preparation). Also, taking advantage of deep XMM-Newton data, X-ray spectral analysis will be given for all sources with sufficient counts within LS, including AGNs (M. Elías-Chávez et al. 2025, in preparation).

The paper is organized as follows: Section 2 presents the observations and sample selection. In Section 3, spectral analysis and fitting details are given. Section 4 shows our AGN-derived parameters, and the analysis is presented in Section 5. In Section 6, a summary listing our main results is provided. Throughout this paper, we use the concordance cosmology with Hubble constants of $H_0 = 70$ km s^{-1} Mpc^{-1}, $\Omega_m = 0.3$, and $\Omega_\Lambda = 0.7$.

2. LS Observations

The details of the LS observations are described in Section 4 of the survey presentation in GO23. In summary, the spectroscopic observations of the faint subset (sources with $20 \leqslant R_C \leqslant 24.5$) were carried out using the OSIRIS instrument at the GTC telescope in MOS mode, hereafter, OSIRIS/GTC. Observations were obtained from 2014 to 2018. The blue region of the spectrum was observed with the R500B grism, which provides a wavelength coverage of 3600–7200 Å and a nominal dispersion of 3.54 Å pixel^{-1}. The red part was covered with two grisms (R500R and R1000R). The former has a wavelength coverage of 4800–10000 Å and a dispersion of 4.88 Å pixel^{-1}, while the latter has a range of 5100–10000 Å and a dispersion of 2.62 Å pixel^{-1}. Table 2 of GO23 provides detailed information about the configuration of the OSIRIS/GTC runs obtained from 2014 to 2018. The data reduction is also described in Section 5 of GO23. Calibrated 1D spectra were used to obtain redshift estimations and detailed information about each object from the spectral analysis. In this work, we selected the OSIRIS/GTC spectra of a sample of Type 1 AGNs identified in the LS survey catalog.

2.1. Sample Selection

From the initial spectroscopic sample of 409 FIR-selected objects from the LS catalog, 69 (17%) AGNs were identified in M. González-Otero et al. (2024). The selection criteria are based on X-ray, FIR, and spectroscopic properties, including the use of diagnostic diagrams given by J. A. Baldwin et al. (1981). All the AGN spectra were visually inspected to select only those showing broad emission lines (BELs), i.e., only Type 1 with an FWHM larger than 1000 km s^{-1}. We obtained a final sample of 30 Type 1 AGNs in a large redshift interval of $0.46 < z < 4.97$.

Table 1 contains the list of Type 1 AGNs considered in this study. GO23 sub-classified 26 of the Type 1 AGNs as X-ray point sources (Xr), 10 as FIR objects, one as a red quasar, and one as a submillimeter galaxy (SMG). Six objects have both FIR and Xr classifications. Object 206653 is a broad absorption line (BAL) quasar. All objects were cross-correlated with the SDSS Data Release 17 (DR17; Abdurro'uf et al. 2022) database, and 12 objects with spectroscopic observations were identified. The redshift distribution of our sample is presented in Figure 1, where we can see a broad z distribution with a maximum of objects around $z \sim 1.8$, nine objects with $z > 2.4$, and only three low-z objects below 0.8. The apparent magnitude in the B band, M_B, is also plotted to show the faintness of our sample. We can see a tendency of the

---

Table 1
Type 1 AGNs Sample

ObjID	R.A. (deg)	Decl. (deg)	z_{spec}	D_L (Mpc)	M_B (mag)	GO23 Class	Fitted Lines	SDSS DR17
(1)	(2)	(3)	(4)	(5)	(6)	(7)	(8)	(9)
78393	162.83676	57.32841	4.9671	46278	−22.79	FIR	Lyα	⋯
206388	163.15096	57.26719	1.7338	13039	−25.97	FIR	C IV, 1900 Å	⋯
206427	163.04043	57.35126	3.2798	28289	−24.89	Xr	Lyα, Si IV, C IV	J105209.70 + 572104.5
206433	163.18630	57.35626	2.8312	23704	−25.60	Xr	Lyα, Si IV, C IV, 1900 Å	J105244.70 + 572122.4
206445	163.51090	57.37629	1.4058	10069	−22.06	Xr, FIR	1900 Å, Mg II	⋯
206473	163.51841	57.41341	1.9717	15268	−23.70	FIR	Si IV, C IV, 1900 Å	⋯
206475	163.38222	57.41506	1.9564	15123	−25.57	Xr	Si IV, C IV, 1900 Å, Mg II	J105331.73 + 572454.0
206479	163.56356	57.41711	4.024	36098	−24.00	Xr	Lyα, C IV	⋯
206482	163.23815	57.41853	1.5309	11186	−23.36	Xr, FIR	1900 Å, Mg II	J105257.14 + 572506.8
206489	163.39600	57.42837	0.7848	4901	−22.13	Xr	Mg II, Hβ	⋯
206510	163.01541	57.45189	2.4334	19735	−21.60	FIR, red QSO	Lyα, C IV	⋯
206512	163.45927	57.45264	1.7237	12946	−24.88	Xr	C IV, 1900 Å, Mg II	J105350.22 + 572709.5
206531	163.28877	57.47232	1.5698	11538	−24.27	Xr, FIR	C IV, 1900 Å, Mg II	J105309.29 + 572820.4
206557	163.10252	57.50262	1.009	6681	−20.76	Xr	Mg II	⋯
206562	163.24654	57.50832	1.676	12507	−22.95	Xr	C IV, 1900 Å	⋯
206570	162.90556	57.51196	0.8922	5739	−20.46	Xr	Mg II	⋯
206579	163.41561	57.51794	0.5855	3427	−22.72	Xr	Mg II, Hβ, Hγ	⋯
206593	163.05521	57.53933	1.873	14337	−24.30	Xr	C IV, 1900 Å	J105213.25 + 573221.5
206597	163.48816	57.54483	1.28	8967	−23.25	Xr, FIR	1900 Å, Mg II	J105357.13 + 573241.4
206623	163.27522	57.57350	2.9514	24922	−26.14	Xr	Lyα, Si IV, C IV, 1900 Å	J105306.04 + 573424.6
206625	162.97661	57.57711	0.877	5619	−22.30	Xr, FIR	Mg II	⋯
206641	163.31984	57.59742	1.2023	8298	−24.83	Xr	1900 Å, Mg II	J105316.76 + 573550.7
206653	163.51091	57.61362	2.6337	21721	−25.39	Xr	Lyα, Si IV, C IV, 1900 Å	⋯
206666	162.90501	57.63184	1.9387	14956	−24.90	Xr, FIR, SMG	Si IV, C IV, 1900 Å, Mg II	J105137.18 + 573754.7
206667	163.26008	57.63248	1.8837	14437	−24.38	Xr	Si IV, C IV, 1900 Å, Mg II	J105302.41 + 573756.8
206672	163.03078	57.64392	2.7267	22652	−24.30	Xr	Lyα, Si IV, C IV	⋯
206679	163.12537	57.65379	1.437	10345	−23.57	Xr	1900 Å	⋯
206692	163.09724	57.68931	1.5326	11201	−23.29	Xr	1900 Å, Mg II	⋯
206695	163.02548	57.69012	0.4619	2577	−20.94	Xr	Mg II, Hβ	⋯
206764	162.93636	57.46886	3.4	29534	−24.10	Xr	Lyα, Si IV, C IV	⋯

Note. The columns are as follows: (1) object identifier in the catalog by GO23, (2) and (3) R.A., decl. (epoch J2000), (4) spectroscopic z_{spec} reported by GO23, (5) luminosity distance in Mpc, (6) absolute magnitude in the B band computed from the SDSS photometric system following K. Jordi et al. (2006), (7) object identification reported by GO23, (8) regions considered for the spectral component fitting, (9) spectra found in SDSS DR17.
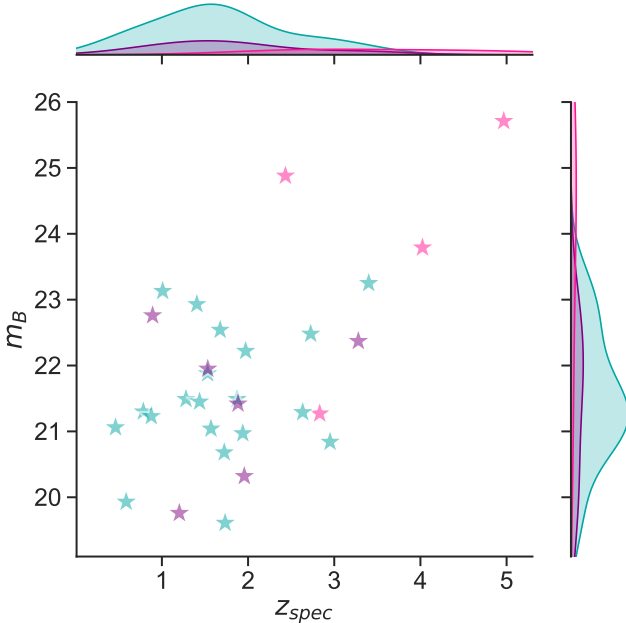

Figure 1. Redshift distribution of Type 1 AGNs in the LS as a function of the apparent magnitude. The color code corresponds to the Class Identification of GO23: FIR in pink, FIR-Xr in purple, and Xr in blue.

FIR objects toward high-z, high-M_B values, while the FIR-Xr and Xr objects are mixed in a lower-z, lower-M_B range.

3. Spectral Analysis

Type 1 AGNs provide information on the kinematics of the gas closest to the SMBH. In addition, the diversity of their emission lines, broad permitted, and semi-forbidden, and high-ionization lines (HILs), intermediate-ionization lines (IILs), and low-ionization lines allows us to infer the composition and physical properties of the emitting gas. Therefore, careful spectral analysis of each emission line is a fundamental step in optical-UV spectroscopic studies (e.g., J. W. Sulentic et al. 2000a; P. Marziani et al. 2010; S. Panda 2024). This section defines the main spectral components in the broad and narrow optical and UV spectra to be considered, depending on different kinematic and physical conditions. We also defined the spectral regions selected for our analysis and their spectral components.

3.1. Methodological Considerations

Spectral analysis of the optical and UV emission lines is performed by separating the virialized BCs from the wind regions, the narrow lines located in an outer region, the
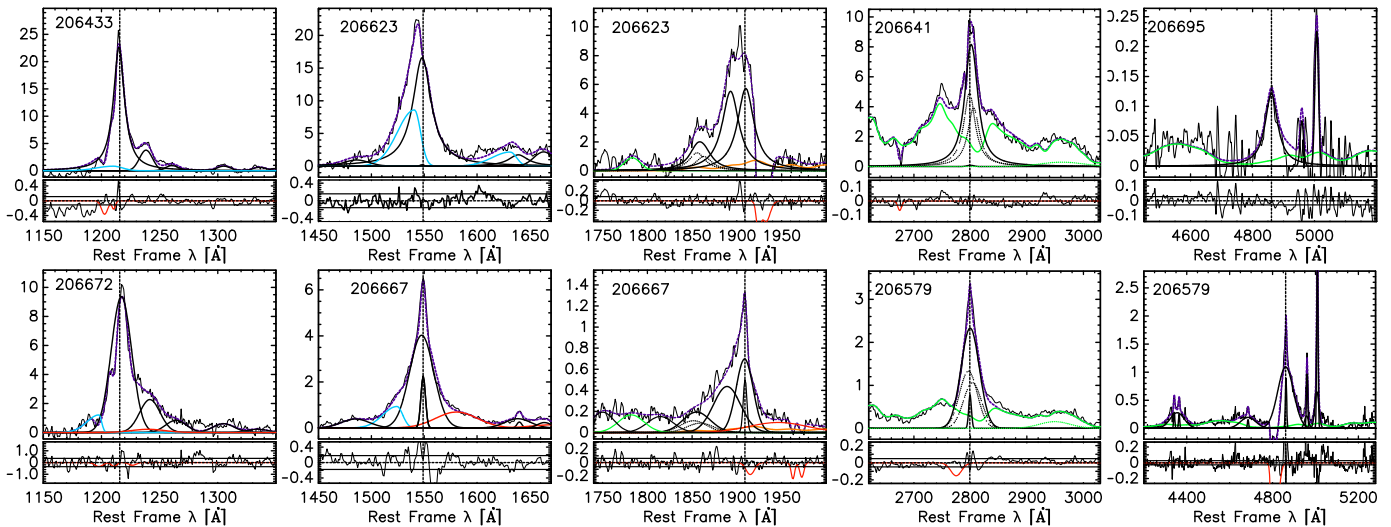
Figure 2. Examples of spectral fitting using Lorentzian (upper panels) and Gaussian (lower panels) profiles for Lyα, C IVλ1549, 1900 Å blend, Mg IIλ2800, and Hβ. The ordinate is the rest-frame wavelength, while the abscissa is the flux in units 10^{-16} erg s^{-1} cm^{-2} Å^{-1}, considering the continuum subtracted. The thin black line represents the observed spectra, thick black lines represent the BC, blueshifted components are in blue, VBC emissions are in red, and narrow lines are in gray. The purple dashed line is the sum of all the fitted components. The vertical dashed line is the rest frame. Green continua in Mg IIλ2800 and Hβ are the Fe II template. In the 1900 Å blend, the Fe III template is shown in orange. The lower panels are the residuals, with red lines showing the absorption lines considered in the fit. The entire figure set, consisting of 73 spectral fits, is available in the online journal.

(The complete figure set (73 images) is available in the online article.)

underlying continuum, and the Fe II pseudo-continuum emission. Our analysis is based on previous works on spectral analysis in the optical (e.g., S. Zamfir et al. 2010; C. A. Negrete et al. 2018; E. Benítez et al. 2023; S. T. Mengistue et al. 2023; H. Ibarra-Medel et al. 2025) and in the UV ranges (e.g., P. Marziani et al. 2013a; C. A. Negrete et al. 2014; M. L. Martínez-Aldama et al. 2018; K. Garnica et al. 2022; T. M. Buendia-Rios et al. 2023), which takes into account the different ionization stages of the broad emitting lines.

Broad Lines. BELs are considered to emerge from the virialized BLR. We assume that these emission lines have a symmetric profile characteristic of Doppler broadening. However, we also consider previous studies suggesting that the BLR emission line profiles may be Gaussian or Lorentzian (e.g., P. Marziani et al. 2010, see also W. Kollatschny & M. Zetzl 2013 for analysis of line profile broadening simulations). The choice of the type of profile to use will be constrained by other spectral features, particularly the FWHM, the intensity of the Fe II in the optical range, and the C IVλ1549 asymmetry in the UV range. BELs with an FWHM $<$ 4000 km s^{-1} are better fitted with a Lorentzian profile since it describes the central emission and the extended wings characteristic of this profile (see Figure 2 of P. Marziani et al. 2010, and Figure 2). Usually, these Lorentzian line profiles are accompanied by strong to moderate Fe II emission in optical and UV emission by prominent C IVλ1549 blue asymmetries. For broader lines with an FWHM $>$ 4000 km s^{-1}, a Gaussian profile adequately represents the virialized component of the BLR (see Figure 2 in P. Marziani et al. 2010, and Figure 2). Gaussian profiles are the choice to fit objects with a faint or null Fe II optical emission and a more symmetric C IVλ1549 profile. We assume that this broad line is the "core" component of the BLR and should be centered in its respective rest frame with a small range of possible shifts within the range of the spectral resolution.

Blue and Redshifted Line Profiles. For the case of IILs and HILs, a blueshifted component associated with outflow winds

is expected (J. W. Sulentic et al. 2007, 2017). This blue component is prominent in the broad lines with an FWHM $<$ 4000 km s^{-1}, specifically in the HILs C IVλ1549, He IIλ1640, and Si IVλ1397 in the UV spectra, and in the narrow lines of [O III] in the optical spectra. The line profile used to fit for the blue component is an asymmetrical Gaussian profile with an FWHM $>$ 6000 km s^{-1} (D. Proga et al. 2000; S. Panda et al. 2019; P. Marziani et al. 2022). For broad lines with an FWHM $>$ 4000 km s^{-1}, a very broad redshifted component (VBC) can also be present in all BELs. The origin of this VBC remains unclear (P. Marziani et al. 2010). Some studies suggest that it can be due to optically thin gas present in quasars with low accretion rates that allows matter to approach the inner edge of the accretion disk, creating a region with gas at very high velocities. This redshifted, VBC emission with an FWHM of $\sim$ 10,000 km s^{-1} can become a very prominent component in some spectra that cannot be attributed to other emitting components (e.g., E. Benítez et al. 2022; T. M. Buendia-Rios et al. 2023).

Iron Emission. Fe II emission is strong in the optical range, as seen in the composite quasar spectrum of D. E. Vanden Berk et al. (2001). This Fe II emission generates a pseudo-continuum, extending from 4000 to 5400 Å, and is the product of the multiplet transitions of the ion (e.g., J. Kovačević et al. 2010; S. T. Mengistue et al. 2023). We will consider the optical Fe II template used in C. A. Negrete et al. (2018) obtained from a high-resolution spectrum of I Zw 1 plus a model of the emission computed by a photoionization code in the Hβ range (see also P. Marziani et al. 2009). The Fe II emission is also blended and strong in the vicinity of Mg IIλ2800 (H. Sameshima et al. 2009; P. Marziani et al. 2013a; R. Prince et al. 2023). In the UV range around 2800 Å, we consider F. Bruhweiler & E. Verner (2008) Fe II emission templates computed from CLOUDY simulations (G. J. Ferland et al. 2009). In the range around the 1900 Å blend, Fe II is not as intense, and we only consider the emission of Fe IIλ1785 (FeIIUV191) as an isolated component. In contrast, the Fe III

emission is intense between 1840 and 2120 Å (C. A. Negrete et al. 2012). For the Fe III multiplets, we used the template of M. Vestergaard & B. J. Wilkes (2001).

Narrow Lines. All permitted and forbidden narrow emission lines were assumed to be created in the external low-density ($\log n_H \sim 4$) narrow-line region. The typical FWHM of these lines is below 1000 km s^{-1}, except for a second blueshifted component of [O III], which can reach up to 2000 km s^{-1} (the semi-broad (SB) component; C. A. Negrete et al. 2018). We assume that all narrow components (NCs) are emitted in the same region and, therefore, share the same kinematics. So, for each fitting range, the same FWHM and offsets were used for all narrow lines in that region.

Continuum. Whenever possible, we fitted a single power law to account for the underlying continuum of the whole spectral range. We use continuum windows around 1280, 1350, 1450, 1700, 2150, 3000, 4440, and 5100 Å (see, e.g., P. J. Francis et al. 1991). A special treatment for the continuum was considered in the Lyα range owing to the Lyα forest (M. Rauch 1998). A series of absorption lines on the blue side of Lyα is expected because of the hydrogen clouds located in our line of sight. To set the continuum under the Lyα range, we assume the continuity of the power law, considering the continuum windows at 1350 Å and 1700 Å.

3.2. Spectral Fitting

We used the IRAF-SPECFIT task (G. Kriss 1994) to perform the spectral fitting. SPECFIT simultaneously fits the emission and absorption line components and the continuum models. It requires selecting a set of functional forms to model the emission and absorption line components, the underlying continuum, and the power-law index. Subsequently, SPECFIT fits the strong BELs, followed by the NCs and Fe II optical pseudo-continuum. SPECFIT can use Gaussian or Lorentzian line profiles by inputting their intensity, central wavelength, and FWHM. Therefore, SPECFIT can model complex line systems, such as the complicated continuum of Fe II, blended emission lines, and extinction. The fit uses a χ^2 minimization with a Marquardt grid fit algorithm from Numerical Recipes (W. H. Press et al. 1986; G. Kriss 1994).

The considerations set in the previous section allow us to constrain the general parameters of spectral lines. We now describe the spectral features associated with the expected physical conditions for the emission lines, which will help us constrain the number of free parameters in the spectral fits. For each spectral range described below, the most intense line was first fitted if more than one emission line was observed within the spectral range. For objects with $z > 2.4$, the most intense line is Lyα; however, this is also the line with the largest absorption. Thus, for objects with $z > 1.28$, the dominant line is C IVλ1549.

Hβ. The spectral range considered was 4440–5400 Å. The continuum was fitted considering the windows at 4440 and 5100 Å, followed by the Fe II pseudo-continuum. We then model the Hβ components BC, NC, and SB of [O III] $\lambda\lambda$4959,5007, considering the theoretical 1:3 ratio (D. E. Osterbrock 1981), and the NC of Hβ. Finally, the fit of He IIλ4687 was included by considering the residuals. For object 206579, the high signal-to-noise ratio (S/N) and spectral coverage allowed the modeling of Hγ to be done together with the fit of Hβ.

Mg IIλ2800. The fitted range is from 2600 to 3050 Å. The continuum was fitted considering both the window at 3000 Å and Fe II UV emission. Mg IIλ2800 is a doublet where we consider a line ratio of I(Mg IIλ2796.35)/I(Mg IIλ2803.53) = 0.8 (P. Marziani et al. 2013a, 2013b). Using the F. Bruhweiler & E. Verner (2008) Fe II template gives us a residual around 2950 Å associated with an emission of Fe I, which we fitted with a Gaussian component. Looking at the residuals, a single Mg IIλ2800 NC was considered to achieve the best fit for some objects.

1900 Å Blend. The main emissions in the spectral range between 1750 and 2000 Å are three IILs: C III]λ1909, Si III]λ1892, Al IIIλ1860. Of particular importance are the C III]λ1909 and Si III]λ1892 lines, as they are broad semi-forbidden lines and have served to constrain the physical parameters in the emitting region, mainly the density and the ionization parameter (C. A. Negrete et al. 2012, 2013, 2014; K. Garnica et al. 2022). The Al IIIλ1860 doublet was fitted using two separate components at 1854.6 and 1862.2 Å and a line ratio 1:1.25. In this region, Fe III emission is also observed, which is particularly intense in objects where Al IIIλ1860 is also intense (see Sections 3.1 and 4). We also expect the contribution of multiplets of Fe II as seen in C. A. Negrete et al. (2014); however, we fitted only the strongest line Fe IIλ1785, as the rest of the lines of the multiplet are much fainter and buried under the blend. Finally, we consider weaker emissions around the blend, such as Si IIλ1816 and N IIIλ1750.

C IVλ1549, He IIλ1640, and Si IVλ1397. As these three lines share high-ionization potentials, they were fitted with the same BC profile, FWHM, shift, and several complementary components that share the same profile (see Section 3). C IVλ1549 and He IIλ1640 were fitted at the same time because the blue side of He IIλ1640 is usually blended with the red wing of C IVλ1549. We model Si IVλ1397 separately because in high-z objects, it lies on the blue edge of the spectra and becomes noisy or with large flux uncertainties. It is well known that the Si IVλ1397 doublet is blended with O IVλ]1402. However, the O IVλ]1402 BC emission is expected to be negligible in comparison to the Si IV emission (Y. Juarez et al. 2009; C. A. Negrete et al. 2012, 2014). We fitted the C IVλ1549 line in the range of 1450–1700 Å, setting the BC of C IVλ1549 in its rest frame, to reach its maximum intensity. Based on the residuals, a blue and/or a redshift component as described in Section 3.1 is considered. Then we fitted He IIλ1640 and other faint lines such as O IIλ1304 and N IVλ1684. Si IV: The λ1400 blend was fitted similarly to the C IVλ1549, in the range of 1350–1450 Å, using those found in C IVλ1549 as initial conditions. We used a BC considering the doublet with individual lines at 1402 and 1394 Å and a flux ratio of $F(1394) = 0.91 \, F(1402)$. In agreement with the C IVλ1549 fit, a blue and/or redshifted component was fitted for some objects.

Lyα Region. In addition to the Lyα components that were fitted based on the emission components and line profiles of C IVλ1549, we also consider modeling N Vλ1240, S IIλ1263, O IIλ1304, and C IIλ1335 lines to obtain a more robust fitting. We used Gaussian profiles to model these extra components, fixing the line shifts and widths of the faintest components to have the same values. The fitting range used is between 1180 and 1350 Å. For objects with absorption produced by the Lyα forest, the range was shortened to 1210–1350 Å, and some

Table 2
Values Used for Computing the M_{BH} Using Equation (1)

Line	Cont (Å)	B.C.	Ref (B.C.)	α	β	Ref (M_{BH})
(1)	(2)	(3)	(4)	(5)	(6)	(7)
Hβ	5100	10.33	R06	0.50	6.91	VP06
Mg II	3000	5.15	R06	0.62	6.75	TN12
Al III	1700	6.3	MS14	0.58	3.24	BR23
C IV	1350	3.5	S17	0.63	3.35	M19

absorption lines were fitted using a Gaussian model to recover the broad line.

4. AGN-derived Parameters

In this section, we report the line profile parameters of our sample along with the derived parameters obtained from the spectral fitting analysis. Individual parameters, like λ_{cent}, f_{line}, FWHM, velocity shifts, and EWs, measured in the spectral regions described in Section 3.2, are provided in Appendix A. The individual computations of the derived parameters (L_{bol}, M_{BH}, and R_{Edd}[18]) are available in Appendix B. The figures showing the fit done in each spectral region can be viewed in the figure set hosted by Figure 2 in the online journal. Figure 2 shows examples of each spectral range covering Lyα, Si IVλ1397, C IVλ1549, 1900 Å blend, Mg IIλ2800, and Hβ for Lorentzian and Gaussian BC profiles.

The SMBH masses (M_{BH}) were estimated using different calibrators compiled from the literature, using virialized BC in different regions of the optical-UV spectrum. We compiled the α and β coefficients of the equation

$$\log M_{BH}, \text{ line}$$
$$= \log \left\{ \left[\frac{(FWHM(line))}{1000 \text{ km s}^{-1}} \right]^2 \left[\frac{\lambda L_\lambda(cont)}{10^{44} \text{ erg s}^{-1}} \right]^\alpha \right\} + \beta \quad (1)$$

from the works of M. Vestergaard & B. M. Peterson (2006, hereafter VP06) for Hβ, B. Trakhtenbrot & H. Netzer (2012, hereafter TN12) for Mg IIλ2800, T. M. Buendia-Rios et al. (2023, hereafter BR23) for Al IIIλ1860, and P. Marziani et al. (2019, hereafter M19) for C IVλ1549. It is important to note that for the M_{BH} computations, considering C IVλ1549 isolates the virialized BC from the wind blueshifted component. Equation 1 computes the M_{BH} using different virial estimators, where λL_λ is the continuum luminosity cont(Å), in a specific continuum window, and FWHM(line) is from the reference line. Table 2 resumes the values used in Equation (1). The references for the bolometric correction (B.C.) are J. W. Sulentic et al. (2017, hereafter S17), P. Marziani & J. W. Sulentic (2014, hereafter MS14), and G. T. Richards et al. (2006, hereafter R06). C. M. Krawczyk et al. (2013) propose later a B.C. = 2.75 in the UV at 2500 Å, using an integrated spectral energy distribution from 1 μm to 2 keV. However, the difference with R06 is not large.

We also computed the Eddington ratio R_{Edd} values, a fundamental parameter underlying the spectral differences in AGNs (Section 5.1, see also, e.g., P. Marziani et al. 2001).

---

[18] $R_{Edd} = L_{bol}/L_{Edd}$ is the Eddington ratio, the ratio of the bolometric luminosity (L_{bol}) and the Eddington luminosity ($L_{Edd} = 1.26 \times 10^8 \ M/M_\odot$ erg s^{-1}).

Table 3 reports the continuum flux values and the derived properties of the sample. For FWHM(BC), $\log L_{bol}$, $\log M_{BH}$, and L_{Edd}, the reported errors include the standard deviation of individual computations. The ranges and median values μ of $\log L_{bol}$ (in erg s^{-1}) are

1. $\log L_{bol,1350} = 46.11–47.87$, $\mu = 47.23$.
2. $\log L_{bol,1700} = 45.98–47.95$, $\mu = 46.84$.
3. $\log L_{bol,3000} = 44.67–47.30$, $\mu = 45.54$.
4. $\log L_{bol,5100} = 45.13–45.80$, $\mu = 45.78$.

In this $\log L_{bol}$ distribution, we see a trend in the increasing $\log L_{bol}$ median values toward the smallest wavelengths, except for $\log L_{bol}$ (5100 Å). This is because the 5100 Å range was obtained from three objects, whereas the 3000 Å range was obtained from 15 objects spanning a wider L_{bol} range.

Figure 3 presents the dispersion of M_{BH} as a function of $\log L_{bol}$ of the individual virial estimators and individual continuum luminosities. We also show the distribution of M_{BH} in the redshift range and the relationship between R_{Edd} and the FWHM of the BCs. Colored dots are the individual computations for each virial estimator. We used star symbols to highlight the average values. For objects with a single value, the colored dot is superimposed on the star, where the lines connecting the dots to the stars show the values associated with an object. We observed a clear trend in the R_{Edd} versus FWHM plot and derived the anticorrelation using the FWHM normalized by 1000 km s^{-1}:

$$\log R_{Edd} = -0.17 \, FWHM_{1000}(BC) + 0.27 \quad (2)$$

with a correlation coefficient of $r_p = -0.7$. The correlation described above is expected, as the M_{BH} that is used to compute R_{Edd} uses the FWHM values. This expected trend is also shown in the lower panel of Figure 3. Both relations, expected and derived, are consistent with the sample distribution, within the errors. However, previous works using M_{BH} derived from X-ray data show a similar trend, which means that the R_{Edd}–FWHM is a statistically true correlation (P. Marziani et al. 2001).

5. Analysis

The optical-UV spectroscopic analysis based on the QMS formalism allowed us to take advantage of the spectral fitting of the emission lines. Each of these lines provides information about the regions where they are emitted, reflecting the gradient of ionization level from the IILs to HILs. Numerous studies have developed different correlations using observed and derived parameters, which are described in this section and will serve as the basis for our analysis. We also consider the FIR-Xr nature of the LS sample.

Regarding previous spectral observations in the LH field, I. Lehmann et al. (2000) reported 43 quasar spectra in the LH observed between 1996 and 1998; 12 of them coincide with those of our sample. However, comparing their estimations with ours was impossible because the fitting methodology is different, and they do not consider all the emission lines used in our analysis.

5.1. LS Type 1 AGNs in the QMS Context

The QMS in the optical bands has been very useful as it traces accretion-rate-dependent trends. Pop A objects show higher accretion rates, lower M_{BH}, and are mostly radio-quiet.

Table 3
Derived Parameters

ObjID (1)	S/N (2)	Profile (3)	FWHM(BC) (4)	$f(1450)$ (5)	$f(1700)$ (6)	$f(3000)$ (7)	$f(5100)$ (8)	$\log L_{\mathrm{bol}}$ (9)	$\log M_{\mathrm{BH}}$ (10)	$\log R_{\mathrm{Edd}}$ (11)
78393	29	L	2057 ± 261	7.64 ± 1.40	⋯	⋯	⋯	47.87 ± 0.16	9.31 ± 0.31	0.56 ± 0.02
206388	12	L	2833 ± 174	1.63 ± 0.20	1.36 ± 0.13	⋯	⋯	46.35 ± 0.15	8.41 ± 0.17	-0.07 ± 0.05
206427	18	L	3283 ± 321	3.10 ± 0.46	2.84 ± 0.43	⋯	⋯	47.32 ± 0.20	9.50 ± 0.22	-0.39 ± 0.16
206433	25	L	3564 ± 240	5.02 ± 0.92	4.18 ± 0.19	⋯	⋯	47.36 ± 0.18	9.25 ± 0.16	0.08 ± 0.04
206445	37	G	6464 ± 225	⋯	3.15 ± 0.14	1.26 ± 0.04	⋯	46.49 ± 0.05	9.29 ± 0.07	-0.85 ± 0.09
206473	21	L	3395 ± 497	1.18 ± 0.12	1.11 ± 0.07	⋯	⋯	46.37 ± 0.12	8.56 ± 0.18	-0.28 ± 0.06
206475	41	G	5635 ± 399	5.37 ± 0.47	5.38 ± 0.25	3.12 ± 0.11	⋯	47.12 ± 0.13	9.53 ± 0.12	-0.42 ± 0.06
206479	10	L	2764 ± 229	5.56 ± 0.92	4.63 ± 0.56	⋯	⋯	47.76 ± 0.20	9.33 ± 0.24	0.20 ± 0.05
206482	16	L	3234 ± 748	2.43 ± 0.31	1.95 ± 0.13	1.33 ± 0.13	⋯	46.49 ± 0.12	8.68 ± 0.29	-0.29 ± 0.06
206489	17	G	9546 ± 376	⋯	⋯	0.87 ± 0.01	0.42 ± 0.03	45.69 ± 0.08	9.25 ± 0.07	-1.70 ± 1.09
206510	6	L	2245 ± 145	0.56 ± 0.10	0.34 ± 0.07	⋯	⋯	46.18 ± 0.26	8.25 ± 0.26	-0.15 ± 0.11
206512	27	G	5901 ± 414	1.56 ± 0.14	1.12 ± 0.07	0.74 ± 0.07	⋯	46.36 ± 0.19	9.13 ± 0.15	-0.85 ± 0.22
206531	31	G	4750 ± 304	3.33 ± 0.23	3.43 ± 0.09	1.88 ± 0.30	⋯	46.67 ± 0.21	9.12 ± 0.15	-0.55 ± 0.12
206557	17	G	4296 ± 99	⋯	⋯	0.57 ± 0.05	⋯	45.67 ± 0.07	8.61 ± 0.11	-1.05 ± 0.39
206562	13	G	9483 ± 232	1.17 ± 0.17	0.61 ± 0.05	⋯	⋯	46.07 ± 0.16	9.32 ± 0.15	-1.30 ± 0.78
206570	12	G	6098 ± 362	⋯	⋯	0.12 ± 0.01	⋯	44.85 ± 0.08	8.40 ± 0.15	-1.70 ± 1.95
206579	37	G	4672 ± 86	⋯	⋯	2.25 ± 0.08	0.79 ± 0.02	45.73 ± 0.05	8.65 ± 0.05	-1.00 ± 0.13
206593	33	G	11788 ± 281	2.29 ± 0.29	1.91 ± 0.06	⋯	⋯	46.58 ± 0.12	9.80 ± 0.10	-1.22 ± 0.51
206597	28	G	6621 ± 160	⋯	⋯	1.00 ± 0.03	⋯	46.17 ± 0.03	9.35 ± 0.05	-1.30 ± 0.26
206623	47	L	3570 ± 141	13.21 ± 0.43	11.32 ± 0.28	⋯	⋯	47.83 ± 0.04	9.60 ± 0.11	0.21 ± 0.01
206625	18	G	4234 ± 90	⋯	⋯	0.60 ± 0.03	⋯	45.54 ± 0.04	8.52 ± 0.06	-1.10 ± 0.22
206641	66	L	2466 ± 99	⋯	⋯	15.59 ± 0.32	⋯	47.30 ± 0.02	9.18 ± 0.06	0.01 ± 0.01
206653	19	G	5821 ± 412	3.92 ± 0.25	3.64 ± 0.13	⋯	⋯	47.20 ± 0.07	9.49 ± 0.11	-0.35 ± 0.04
206666	29	G	7381 ± 436	$3.60 \ 0.16$	3.12 ± 0.10	⋯	⋯	46.82 ± 0.05	9.65 ± 0.07	-0.89 ± 0.10
206667	13	G	5480 ± 763	0.94 ± 0.09	0.55 ± 0.06	0.67 ± 0.08	⋯	46.17 ± 0.24	9.02 ± 0.26	-0.85 ± 0.28
206672	15	G	5260 ± 583	1.75 ± 0.11	1.33 ± 0.12	⋯	⋯	46.84 ± 0.10	9.32 ± 0.18	-0.66 ± 0.12
206679	22	G	5500 ± 277	⋯	0.70 ± 0.08	⋯	⋯	45.98 ± 0.05	8.68 ± 0.16	-0.80 ± 0.16
206692	18	L	3963 ± 176	2.15 ± 0.18	3.16 ± 0.10	1.03 ± 0.25	⋯	46.54 ± 0.23	8.90 ± 0.18	-0.40 ± 0.14
206695	13	L	2435 ± 379	⋯	⋯	0.38 ± 0.01	0.33 ± 0.02	44.90 ± 0.08	7.59 ± 0.18	-0.80 ± 0.14
206764	15	L	2390 ± 128	2.75 ± 0.79	⋯	⋯	⋯	47.16 ± 0.25	9.06 ± 0.33	0.07 ± 0.11

Note. Column (1) is the object identification. Column (2) is the largest S/N value around the given continuum window of the following four columns. Column (3) is the adopted line profile, Column (4) is the FWHM average values of the BCs in kilometers per second. Columns (5)–(8) are the continuum flux in units 10^{-16} erg^{-1} s^{-1} cm^{-2} Å^{-1}. Columns (9) and (10) are the average values of the logarithm of the L_{bol} and M_{BH}, and column (11) is the average value of the R_{Edd}.

A classification in subbins has been proposed to group objects with similar spectra and, thus, physical conditions. Pop A1, A2, A3, and A4 are defined in terms of increasing Fe II emission in bins of $\Delta R_{\mathrm{Fe\,II}} = 0.5$. Objects in the A3–A4 subbins are identified as extreme accretors (xA quasars) in the sense that their accretion rate is close to the Eddington limit. Pop B objects have low accretion rates, much higher M_{BH} and are mostly radio-loud quasars. Populations in the subbins B1, B1+, and B1++ are defined in terms of increasing ΔFWHM = 4000 km s^{-1} (P. Marziani et al. 2010).

In the ultraviolet range, computing the half-height centroid $c_{(1/2)}$ of C IVλ1549 (see Section 5.3, Equation 3) is not a straightforward task for large samples, as the line should be cleaned first from the extra emission, mostly the C IVλ1549 NC and He IIλ1640. Therefore, we considered the work of P. Marziani & J. W. Sulentic (2014), who showed that using line ratios in the UV could be useful to detect highly accreting objects (see also M. L. Martínez-Aldama et al. 2018; K. Garnica et al. 2022; T. M. Buendia-Rios et al. 2023; N. Jenaro-Ballesteros 2023). The UV diagram involves line ratios of the IILs of the 1900 Å blend, C III]/Al III, and Al III/Si III]. This UV diagram also allows the identification of objects with high (C III]/Al III < 1) and low (C III]/Al III > 1) accretion rates, as well as xA objects (C III]/Al III < 1 and C III]/Al III > 0.5).

Using our spectral measurements, we reproduced the optical QMS for the three objects at $z < 0.8$ and compared the results with archival data from S. Zamfir et al. (2010) and C. A. Negrete et al. (2018). The upper panel of Figure 4 shows the optical QMS with the objects in LS shown as green stars (the three objects are classified as Xr sources). Two belong to Pop B and one to the Pop A region. None of them were in the xA domain.

For the UV range, we compiled spectroscopic information from M. L. Martínez-Aldama et al. (2018), J. W. Sulentic et al. (2014), C. A. Negrete et al. (2014), and T. M. Buendia-Rios et al. (2023, 2025) to build the C III]λ1909/Si III]λ1892 versus Al IIIλ1860/Si III]λ1892 diagram (shown in the middle panel of Figure 4). In this UV QMS, the 18 LS objects showing the 1900 Å blend fall into the Pop B region, with three objects at the boundary of Pop A. In this subsample, we have one FIR object that, together with a FIR-Xr object, falls in the higher part of the C III]λ1909/Si III]λ1892 values. Of the remaining nine objects, three only have Mg II emission. Taking into account the analysis of P. Marziani et al. (2013a, 2013b) that uses the FWHM as a tracer of the population membership, the three objects are Pop B. The other five objects have C IVλ1549 emission, four with Lorentzian profiles (and then are Pop A objects) and one with a Gaussian profile (a sign of a Pop B object). Finally, one spectrum has only Lyα emission with a Lorentzian profile, so it could be considered a Pop A object. In summary, we have 25 Pop B and five Pop A objects.
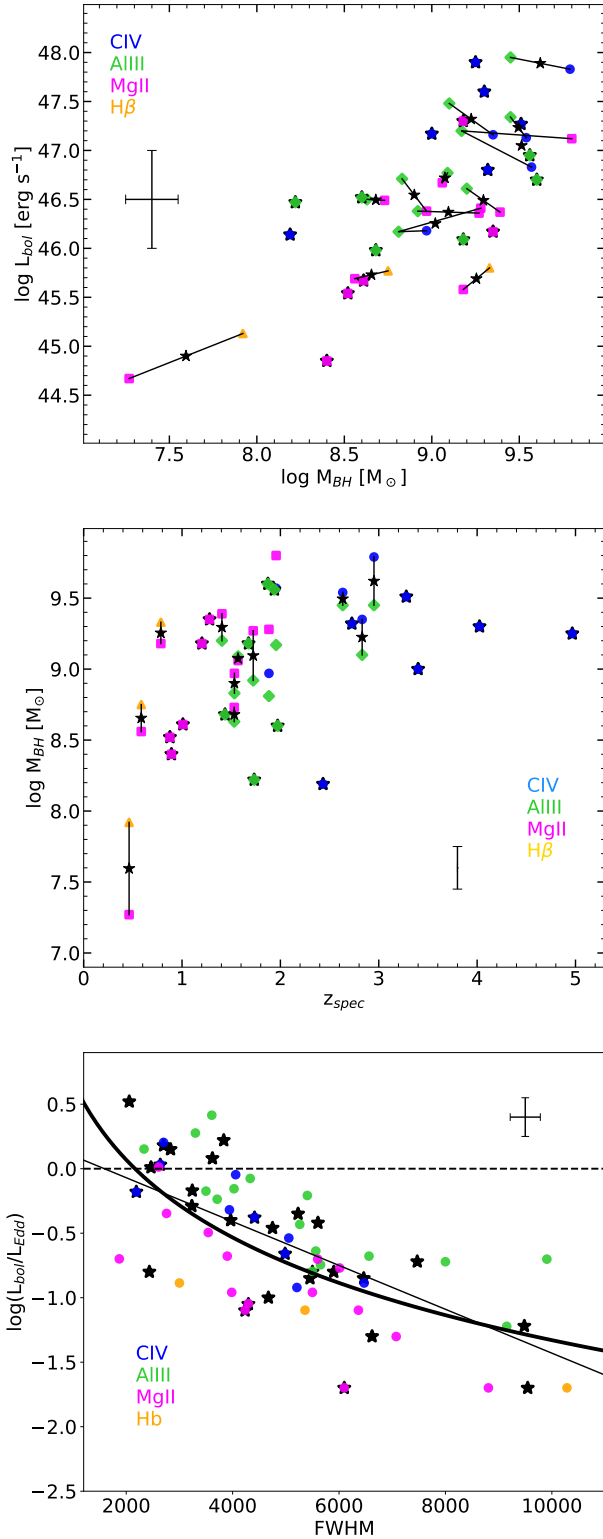
Figure 3. Distributions of $\log M_{\rm BH}$—$\log L_{\rm bol}$ (upper panel), $\log M_{\rm BH}$ in the z-range (middle panel), and $\log R_{\rm Edd}$–FWHM(BC) (lower panel). In the lower panel, the dashed horizontal line corresponds to $R_{\rm Edd} = 1$, the solid thin line represents an anticorrelation between both quantities, and the solid thick line is the expected correlation of $R_{\rm Edd}$ and the FWHM. The average error bars are also shown.

Figure 4. QMS in the optical (upper panel) and UV (middle panel). The vertical dashed lines are the boundary for xA objects. The horizontal dashed lines are the boundary separation of Pops. A and B. Lower panel: relation between $R_{\rm Mg\,II}$ and $R_{\rm Edd}$. The meanings of the symbols are described in the inner boxes. filled gray circles are low-z data from J. Shin et al. (2021), and the color code background is the redshift distribution of the SDSS DR17 sample taken from Q. Wu & Y. Shen (2022).

5.2. Fe II in the UV

The lower panel of Figure 4 shows the relationship between Fe II UV/Mg II ratio ($R_{\rm Mg\,II}$) and $R_{\rm Edd}$ of the 16 objects showing Mg II (five FIR-Xr and 11 Xr sources). We compare
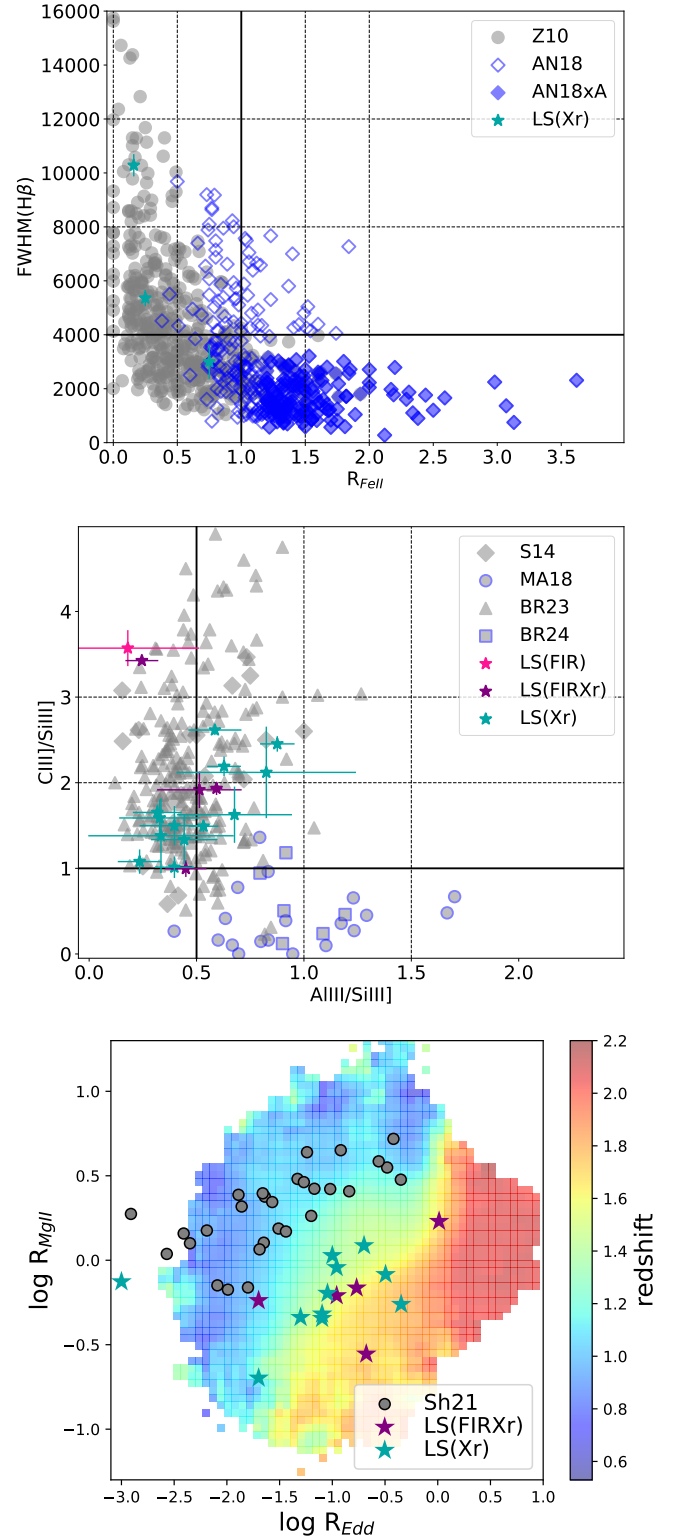
the values of the objects in our sample, whose z-range is between 0.46 and 1.96, with two other samples. The first is from the work of J. Shin et al. (2021, hereafter Sh21, filled

gray circles), who used 29 objects observed by the Hubble Space Telescope at $z < 0.37$ (with a mean value of 0.04). Sh21 explained the scenario of the close correlation between $R_{Mg\,II}$ and R_{Edd} as a consequence of metal cooling, leading to an increase in the gas inflow and, consequently, the accretion rate. The second sample corresponds to the SDSS DR17 quasar catalog properties of Q. Wu & Y. Shen (2022, shown in color code). From this second sample, we consider spectra with an $S/N > 5$ in the integrated G band, which is the minimum value of our sample, and $\log L_{bol} > 40$, which is a similar range to our sample. In addition, we define a redshift range from $0.53 < z < 2.2$. This range assures that the spectral regions of Fe II UV and Mg II are visible within the SDSS DR17 spectral range. We obtained a selection of 208,000 objects. As reported by Sh21 (see their Figure 3), we cannot find a redshift dependency with the $R_{Mg\,II}$ ratio for the SDSS DR17 quasars. However, we find a clear redshift dependency on the $R_{Mg\,II}$–R_{Edd} relation: the latter decreases as the redshift increases. This implies a trend in the R_{Edd}, where at lower z we find lower values of R_{Edd}, and vice versa, at higher z we have higher values of R_{Edd}. In other words, there is a family of $R_{Mg\,II}$–R_{Edd} relations dependent on z. When we compare with our sample, the $R_{Mg\,II}$–R_{Edd} relation is in agreement with the SDSS DR17 quasars within our redshift range, showing a clear linear relation between $R_{Mg\,II}$ and R_{Edd}, but with the expected offset from the Sh21 relationship.

5.3. Winds in the LS Sample?

One of the most important properties of Type 1 AGNs is the presence of winds arising from the central region, derived by accretion mechanisms (e.g., M. Elvis 2000). In the BLR, these winds are mainly detected in HILs, such as C IVλ1549, reaching velocities up to -2500 km s^{-1} (G. T. Richards et al. 2011; Q. Wu & Y. Shen 2022). G. T. Richards et al. (2011) showed a relationship between the EW and the total shift of the C IVλ1549 line profile, which is argued to be driven by accretion parameters. It is worth noting that the approximation in the works that considers thousands of spectra is based on automatic fits to the emission lines, and the reported blueshift velocities correspond to the total C IVλ1549 emission.

Our approximation considers the QMS formalism, where particular initial conditions were considered for different populations, assuming two different emitting regions. (see Section 3.1). The isolated blueshifted C IVλ1549 component has been reported in numerous previous works (e.g., P. Marziani et al. 2010; J. W. Sulentic et al. 2017; M. L. Martínez-Aldama et al. 2018; Buendia-Rios et al. 2025 submitted, and references therein).

Another parameter for quantifying the C IVλ1549 blueshift is the half-height centroid $c(1/2)$, defined as

$$c(1/2) = \frac{v_{r,R}(1/2) + v_{r,B}(1/2)}{2} \qquad (3)$$

where $v_{r,R}$ y $v_{r,B}$ are the velocity shifts on the red and blue wings at half-height, respectively (S. Zamfir et al. 2010). Upper panel of Figure 5 shows the distribution of $c_{(1/2)}$ versus FWHM (C IVλ1549) from our sample (LS), compared with samples of J. W. Sulentic et al. (2007, hereafter S07) for low-z objects, and J. W. Sulentic et al. (2014, 2017, hereafter S14, S17) for high-z quasars, for faint and bright samples, respectively. In S07 and S17 samples, the tendency to find winds in C IVλ1549 with
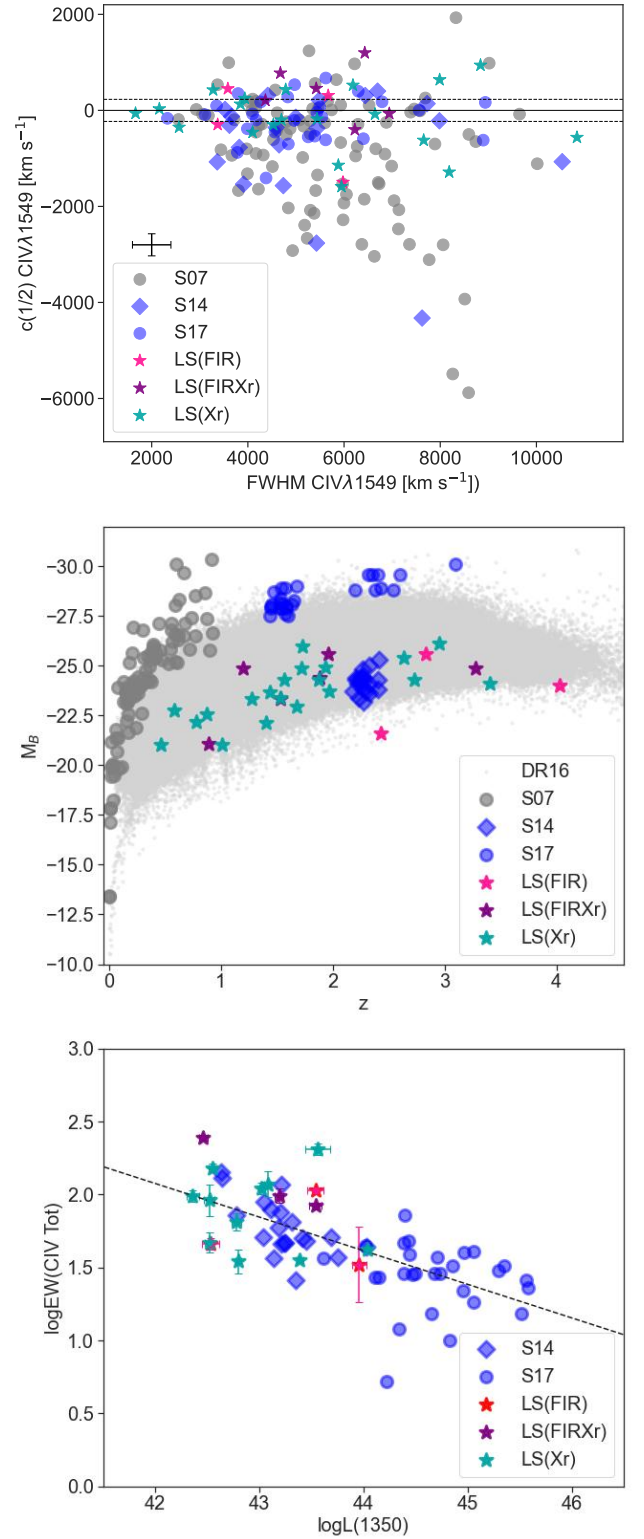
Figure 5. (Upper panel) Dependence of the velocity shift at half intensity of C IVλ1549, $c_{(1/2)}$ on FWHM(C IVλ1549). The solid line is the reference for zero velocity shift. The dashed lines represent the uncertainty range with respect to zero velocity shift. (Middle panel) Absolute B-magnitude M_B vs. redshift z. (Lower panel) BE. The dashed line shows the linear fit of our data (Equation (4)). The meanings of the symbols are described in the inner boxes.

$c_{(1/2)}$ blueshifts above -4000 km s^{-1} is noticeable. Winds become less prominent in the S14 and LS samples with blueshifts below -1200 km s^{-1}. The LS sample has similar z and

$\log L_{\rm bol}$ ranges as the S14 and S17 samples. However, the S14 sample was selected considering the flux limits of the LS sample at the highest possible z. On the other hand, the S17 sample was chosen from the Hamburg ESO (HE; L. Wisotzki et al. 2000) sample as the brightest blue objects at a similar z-range to S14. Bluer, brighter quasars at high-z tend to show blueshifts in the HILs. The middle panel of Figure 5 compares the z–M_B relation from the S07, S14, S17, and LS samples, showing that our sample shares a similar M_B magnitude range as the S14 sample, including similar spectral properties. For completeness, we also included the absolute magnitudes from the SDSS DR17 data taken from Q. Wu & Y. Shen (2022). In both figures, we do not find any clear tendency with the FIR-Xr classification, except for the one with z mentioned in Section 2.1.

Finally, in the optical range, [O III]$\lambda\lambda$4959,5007 is the HIL that traces these winds (R. Zamanov et al. 2002; C. A. Negrete et al. 2018; G. Grünwald et al. 2023). Optical winds are identified by the presence of a second SB [O III]$\lambda\lambda$4959,5007 component shifted to the blue, in addition to the typical NC positioned in the rest frame. The [O III] SB wind component can have an FWHM up to 2000 km s^{-1} and blueshifts up to -2000 km s^{-1} with respect to the rest frame (C. A. Negrete et al. 2018). In quasar spectra, SB [O III]$\lambda\lambda$4959,5007 components with offsets larger than -250 km s^{-1} are considered optical outflows (R. Zamanov et al. 2002). In our sample, only one object shows a second semi-BC with an FWHM of 1350 ± 100 km s^{-1}. It has a shift of -25 ± 27 km s^{-1}; therefore, it cannot be considered a wind component.

5.4. Baldwin Effect

The anticorrelation between the EW of C IVλ1549 and the continuum luminosity in high-z UV spectra is known as the Baldwin effect (BE; J. A. Baldwin 1977). The BE arises from the relationship between the total line flux over the underlying continuum flux and the underlying continuum luminosity, so the correlation is expected. However, as reported in previous works, the slope of the BE relation is not unity, indicating that the line luminosity does not change by the same amount as the underlying continuum does (e.g., W. Zheng & M. A. Malkan 1993; Y. Wang et al. 2022). The origin of the BE relationship has also been discussed in terms of the Eddington ratio. R. Bachev et al. (2004, see also X. Ge et al. 2016) considered UV spectra within the QMS analysis, finding a systematic decrease of the C IVλ1549 EW as the $R_{\rm Edd}$ decreases, suggesting that the origin of the C IVλ1549 BE is the $R_{\rm Edd}$ itself.

The slope on the BE has been reported to be around -0.24 along a wide range of redshifts. For instance, W.-H. Bian et al. (2012), using SDSS DR7 with 35,000 quasars in a redshift range from 1.5 to 5, obtained a slope of -0.238. The lower panel of Figure 5 shows the BE relation for our sample compared with the high-z samples of S14 and S17. For this analysis, we do not consider the S07 sample as they do not report individual values of the EW(C IVλ1549). As discussed in Section 5.3, our sample shares properties similar to the S14 sample and falls in the same region in the BE diagram. We also do not find any tendency with the FIR-Xr classification. The relationship that we obtain, including S14, S17, and our

sample, is

$$\log {\rm EW(C\ IV)} = (-0.23 \pm 0.03)\log L(1350) + (11.75 \pm 0.23) \tag{4}$$

with a p-value of -0.67. These values are consistent with the values reported in the literature (e.g., W.-H. Bian et al. 2012).

5.5. Comparison with SDSS Data

Given the variable nature of quasars, we searched for the spectra of our sample in SDSS DR17. We found 10 of these with an observation range between 2014 and 2016, except for object 206641, which was observed in 2002. The observation range coincides with that of the LS observations (between 2014 and 2018; GO23). The main difference between SDSS and LS data is that the SDSS spectra have a higher resolution but a lower S/N. Column (9) of Table 1 lists the objects found in SDSS DR17.

We then applied the same criteria and fitting methodology to the spectra observed with our LS sample for the spectral fitting. Then, we look for a one-to-one correlation between the results obtained from the SDSS spectra and our LS sample. It is worth noting that these results can be affected mainly by the low S/N of SDSS spectra. The purpose is to look for evidence of variability that may be due to important changes in the physics of the nuclear region.

The line luminosities correlation ($L_{\rm line}$, which considers BC line luminosities of Lyα, Si IV, C IV, C III], Al III, and Mg II) is close to the one-to-one relation with an offset of -0.20 ± 0.24. Therefore, we found a systematic shift between SDSS and LS values of 0.2 dex. However, once the offset error is considered, the SDSS values can be recovered within 1σ of error. In the case of $L_{\rm bol}$ (in the continuum windows 1350 Å, 1700 Å, and 3000 Å) and FWHM of the BCs of Lyα, Si IV, C IV, C III], Al III, and Mg II) comparisons, the offsets are -0.04 ± 0.28 and -50 ± 820, respectively. Considering the errors, we can conclude that $L_{\rm line}$, $L_{\rm bol}$, and the FWHM from the SDSS and LS values are consistent. In addition, we did not find indications of variability between the two samples once scatter was considered.

5.6. Extinction Analysis

We examine the effects of extinction in our Galaxy on the flux estimations of quasars. For this purpose, we compare the colors $g_{\rm AB} - r_{\rm AB}$ of our quasar LS sample (located around $57°.5$ in decl.) with other quasar samples taken from SDSS DR17 in the Galactic plane (between $\pm 15°$ in decl., group Galactic plane), and the Galactic north pole (above $60°$ in decl., group north pole). We restrict the three quasar sample to a redshift around $z = 1$–2 since most of our LS objects are in this range (see Figure 1). The average color $g_{\rm AB} - r_{\rm AB}$ for the corrected and noncorrected extinction (following the J. A. Cardelli et al. 1989, extinction law) of the three groups is:

1. *LS*. 0.233 ± 0.299; dered 0.213 ± 0.276.
2. *Galactic plane*. 1.145 ± 0.723; dered 0.200 ± 0.358.
3. *North pole*. 0.195 ± 0.228; dered 0.174 ± 0.227.

In conclusion, the current extinction corrections are reliable, especially for objects in the galactic plane, since we can recover the color values.

6. Summary

This paper describes the characteristics of Type 1 AGNs identified by the LS project. We present high-quality spectra of 30 quasars with a redshift range of 0.462–4.967. A detailed spectral fitting method based on the QMS phenomenology prescription was applied to deconvolve the Hβ, Mg II, 1900 Å blend, C IVλ1549, Si IVλ1397, and Lyα regions found in the spectra of the sample. The overall characteristics of the sample are as follows:

1. $\log L_{\rm bol}$: 44.85–47.87.
2. $\log M_{\rm BH}$: 7.59–9.80.
3. $\log R_{\rm Edd}$: −1.70 to 0.56.
4. M_B: −20.46 to −26.14.

The detailed optical-UV spectral splitting allows us to perform different analyses based on correlations of the emission line parameters, properties, and physical conditions of the emission regions reported in previous studies, as described below.

1. We found a wide spectral diversity in our sample from the QMS analysis using optical and UV emission lines. The low-z sample (three objects) falls in Pop A2, B1, and B1+, while quasars of the high-z sample, 23 are Pop B and four Pop A objects. None of the LS quasars was found in the xA domain.
2. We reproduced the relationship between the Eddington ratio $R_{\rm Edd}$, the fundamental parameter underlying the spectral differences in AGNs and the FWHM of the virial components, with an anticorrelation described by $\log R_{\rm Edd}$ = –0.17 FWHM$_{1000}$(BC) + 0.27, with a correlation coefficient r_p = –0.7, similar to that reported by P. Marziani et al. (2001).
3. Using the measurements of the spectra showing Mg IIλ2800 (in the range of 0.462 $> z >$ 1.956), we recovered the relation $R_{\rm Edd}$-$R_{\rm Mg\,II}$, consistent with the results of Sh21, for objects with $z < 0.37$) and the SDSS DR17 quasar catalog sample in a z-range similar to the LS.
4. We also looked for signs of winds in spectra showing the HIL C IVλ1549 in the UV. We computed its half-height centroid $c_{(1/2)}$ as a proxy for the blueshift of the line, finding values of the $c_{(1/2)}$ between 941 and –1587 km s^{-1}. Compared with the other low- and high-z samples of S07, S14, and S17, the LS quasars follow the trends of the S14 sample, which shares a similar range of z and absolute magnitudes.
5. We also consider the anticorrelation of the BE. We find a trend in terms of log L(1350) versus log C IV(EW), with a slope of –0.23 ± 0.03 dex, similar to that reported in the literature, especially by W.-H. Bian et al. (2012), who used the SDSS DR 16 quasar catalog sample.
6. We find 12 spectra of our sample in the SDSS DR17 archive, for which we use the same spectral fitting methodology as with the LS spectra. The principal difference between the SDSS and LS spectra is the low S/N ratio of the former. We found no evidence of spectral variability when comparing values of line luminosities, FWHM, and bolometric luminosities.
7. Finally, we perform an extinction analysis comparing the $g_{\rm AB}$ − $r_{\rm AB}$ colors of our sample with an SDSS DR17 quasar sample. The effects of extinction in the LS field are similar to those in the Galactic north pole, while using the extinction law of J. A. Cardelli et al. (1989) allows recovery of dereddened colors for objects in the Galactic plane.

It is worth noticing that despite the LS sample was selected for the large emission in the FIR using Herschel data at 100 and 160 μm, and X-ray data; we found no evidence of different behavior from those AGNs in nonobscured or with different criteria selected samples, such as SDSS.

---

[19] https://www.sdss.org/

Appendix A
Line Profile Measurements

Tables A1–A6 show output parameters from the SPECFIT fitting procedure described in Section 3.2.

Table A1
Line Component Values for the Lyα Range

	Lyα BC					Lyα Blue					Lyα VBC				
ObjID	Flux[a]	λ_{cent}^{b}	Shift[c]	FWHM[c]	EW[b]	Flux[a]	λ_{cent}^{b}	Shift[c]	FWHM[c]	EW[b]	Flux[a]	λ_{cent}^{b}	Shift[c]	FWHM[c]	EW[b]
78393	215.90 ± 28.09	1215.5 ± 0.4	−43 ± 109	2057 ± 261	39.3 ± 5.1	...	...	...	...	...	...	...	...	...	...
206479	344.10 ± 29.43	1216.2 ± 0.6	139 ± 135	2826 ± 252	60.8 ± 4.4	...	...	...	...	...	...	...	...	...	...
206764	656.56 ± 16.83	1216.5 ± 0.1	194 ± 32	2419 ± 76	276.8 ± 2.8	...	...	...	...	...	...	...	...	...	...
206427	317.21 ± 5.47	1213.8 ± 0.2	−465 ± 37	2514 ± 80	87.5 ± 0.9	...	...	...	...	...	...	...	...	...	...
206623	1545.38 ± 55.96	1215.5 ± 0.2	−51 ± 49	3433 ± 64	96.4 ± 2.2	389.55 ± 30.01	1207.9 ± 0.7	−1921 ± 170	7165 ± 481	24.0 ± 1.2	...	...	...	...	...
206433	406.42 ± 55.39	1215.0 ± 0.0	−165 ± 0	2809 ± 366	108.9 ± 13.9	23.53 ± 0.00	1210.0 ± 0.0	−1398 ± 0	8373 ± 8164	6.4 ± 0.0	...	...	...	...	...
206672	206.10 ± 13.82	1217.1 ± 0.4	359 ± 90	5088 ± 225	97.1 ± 4.4	19.26 ± 3.35	1197.9 ± 0.8	−4372 ± 189	6200 ± 0	8.8 ± 1.1	7.84 ± 27.00	1240.0 ± 10.0	6000 ± 2465	8076 ± 1031	3.8 ± 8.7
206653	528.85 ± 52.89	1215.7 ± 0.0	7 ± 0	6570 ± 275	92.0 ± 0.0	...	...	...	...	...	...	...	...	...	...
206510	28.68 ± 3.71	1215.0 ± 0.0	−165 ± 0	2300 ± 115	37.3 ± 2.1	15.44 ± 0.00	1210.0 ± 0.0	−1398 ± 0	6700 ± 995	19.1 ± 0.0	...	...	...	...	...

	N Vλ1240					SI IIλ1263				
ObjID	Flux[a]	λ_{cent}^{b}	Shift[c]	FWHM[c]	EW[b]	Flux[a]	λ_{cent}^{b}	Shift[c]	FWHM[c]	EW[b]
78393	79.08 ± 6.64	1231.7 ± 0.5	−2045 ± 108	2999 ± 158	14.5 ± 1.2	31.80 ± 3.16	1253.2	−2222	2999	5.8 ± 0.6
206479	84.22 ± 8.87	1240.4 ± 0.8	59 ± 195	4170 ± 441	15.2 ± 1.3	21.50 ± 5.56	1261.0	−378	4170	3.9 ± 0.8
206764	38.27 ± 4.85	1240.9 ± 0.5	186 ± 110	3556 ± 315	17.4 ± 0.8	15.68 ± 3.40	1263.4	185	3556	7.6 ± 0.6
206427	44.92 ± 2.47	1236.6 ± 0.4	−853 ± 104	4078 ± 228	12.8 ± 0.4	10.69 ± 1.39	1259.0	−854	4078	3.1 ± 0.2
206623	382.87 ± 15.74	1236.8 ± 0.3	−820 ± 79	3952 ± 124	24.9 ± 0.6	104.54 ± 8.73	1259.1	−821	3952	7.0 ± 0.3
206433	52.70 ± 5.59	1238.3 ± 0.4	−454 ± 94	3174 ± 31	14.3 ± 1.4	13.31 ± 1.30	1260.7	−455	3174	3.6 ± 0.3
206672	50.06 ± 13.20	1241.6 ± 1.0	354 ± 251	5000 ± 0	24.4 ± 4.2	18.85 ± 4.06	1264.1	353	5000	9.5 ± 1.3
206653	183.62 ± 17.97	1236.2 ± 1.2	−958 ± 283	5549 ± 668	32.8 ± 2.3	46.17 ± 7.37	1258.6	−958	5549	8.5 ± 1.0
206510	15.44 ± 2.80	1237.0 ± 1.3	−759 ± 325	3000 ± 488	21.6 ± 1.6	4.41 ± 1.70	1259.4	−760	3000	6.7 ± 0.9

	O Iλ1307					C IIλ1335				
ObjID	Flux[a]	λ_{cent}^{b}	Shift[c]	FWHM[c]	EW[b]	Flux[a]	λ_{cent}^{b}	Shift[c]	FWHM[c]	EW[b]
78393	42.03 ± 3.14	1302.0	−1095	2999	7.7 ± 0.6	48.96 ± 3.37	1326.4	−1995	2999	9.0 ± 0.6
206479	23.80 ± 5.46	1305.0	−418	4170	4.5 ± 0.8	10.07 ± 4.80	1334.0	−292	4170	1.9 ± 0.7
206764	28.98 ± 3.63	1307.6	187	3556	16.0 ± 0.6	11.77 ± 2.66	1336.1	185	3556	7.0 ± 0.4
206427	12.44 ± 1.35	1303.1	−853	4078	3.9 ± 0.2	5.76 ± 1.24	1331.5	−854	4078	1.8 ± 0.2
206623	65.20 ± 7.06	1303.9	−110	3952	4.7 ± 0.3	55.75 ± 6.95	1335.3	0	3952	4.2 ± 0.3
206433	12.28 ± 1.70	1305.2	192	3174	3.3 ± 0.4	9.33 ± 1.66	1336.2	202	3174	2.5 ± 0.4
206672	14.03 ± 1.62	1305.0	149	5000	7.4 ± 0.5	5.27 ± 1.53	1334.0	−292	5000	2.9 ± 0.5
206653	17.93 ± 5.14	1304.4	0	5549	3.5 ± 0.7	9.19 ± 5.14	1335.3	0	5549	1.8 ± 0.7
206510	4.41 ± 1.77	1304.0	−80	3000	7.8 ± 1.0	4.41 ± 1.49	1335.3	0	3000	8.7 ± 0.8

Note. ([a]) Fluxes are in units ×10⁻¹⁶ erg s⁻¹ cm⁻¹ Å⁻¹. ([b]) Central λ of the fitted component and EWs are in units of angstom. ([c]) Line shifts and FWHM are in units of kilometers per second; as we have low-resolution spectra, the values should be rounded to the nearest tens.

Table A2
Line Component Values for the Si IV λ1397 Range

ObjID	Si IV λ1397 BC					Si IV λ1397 Blue					Si IV λ1397 VBC				
	Flux[a]	λ_{cent}^{b}	Shift[c]	FWHM[c]	EW[b]	Flux[a]	λ_{cent}^{b}	Shift[c]	FWHM[c]	EW[b]	Flux[a]	λ_{cent}^{b}	Shift[c]	FWHM[c]	EW[b]
206764	56.42 ± 1.26	1399.7 ± 0.3	257 ± 71	2113 ± 194.0	31.9 ± 0.3	⋯	⋯	⋯	⋯	⋯	⋯	⋯	⋯	⋯	⋯
206427	25.63 ± 1.68	1396.6 ± 1.0	−411 ± 206	2922 ± 548.0	15.7 ± 0.6	⋯	⋯	⋯	⋯	⋯	⋯	⋯	⋯	⋯	⋯
206623	256.95 ± 8.11	1401.7 ± 1.1	678 ± 246	3182 ± 101.0	11.6 ± 0.2	111.91 ± 12.96	1391.0 ± 0.9	−860 ± 193	5901 ± 878	5.0 ± 0.3	⋯	⋯	⋯	⋯	⋯
206433	72.68 ± 2.32	1400.2 ± 1.2	358 ± 247	4207 ± 239.0	19.4 ± 0.6	2.47 ± 5.08	1394.9 ± 1.9	−18 ± 407	4293 ± 1122	0.7 ± 1.3	⋯	⋯	⋯	⋯	⋯
206672	18.24 ± 2.30	1400.3 ± 1.7	380 ± 372	5704 ± 934.0	10.9 ± 0.7	4.88 ± 2.00	1387.7 ± 0.9	−2637 ± 193	8358 ± 1293	2.8 ± 0.6	4.83 ± 2.93	1425.3 ± 3.0	5417 ± 639	8252 ± 2063	3.0 ± 0.9
206653	85.74 ± 9.14	1398.5 ± 2.6	0 ± 549	5754 ± 913.0	18.4 ± 1.2	⋯	⋯	⋯	⋯	⋯	⋯	⋯	⋯	⋯	⋯
206473	80.54 ± 6.40	1401.0 ± 6.1	532 ± 1319	3700 ± 905.0	19.9 ± 5.0	⋯	⋯	⋯	⋯	⋯	⋯	⋯	⋯	⋯	⋯
206475	57.30 ± 8.58	1399.0 ± 0.0	102 ± 0	5726 ± 641.0	9.3 ± 1.5	4.62 ± 14.79	1378.0 ± 0.0	−4711 ± 0	7258 ± 1002	0.8 ± 2.6	19.93 ± 11.04	1430.9 ± 10.6	6612 ± 2270	8147 ± 4872	3.3 ± 1.9
206666	53.64 ± 0.67	1399.0 ± 0.0	102 ± 0	7116 ± 442.0	15.8 ± 0.2	4.99 ± 6.49	1376.5 ± 1.3	−5041 ± 278	7999 ± 446	1.5 ± 1.7	9.32 ± 2.79	1431.4 ± 9.4	6723 ± 2001	11214 ± 1683	2.8 ± 0.7
206667	22.10 ± 0.76	1399.0 ± 0.0	102 ± 0	5560 ± 507.0	23.8 ± 0.3	3.28 ± 0.83	1370.1 ± 2.0	−6412 ± 434	5901 ± 534	3.3 ± 0.4	3.30 ± 1.25	1440.0 ± 5.0	8566 ± 1071	8965 ± 1533	3.9 ± 0.5

Note. a, b, and c indices have the same meanings as those in Table A1.

14

Table A3
Line Component Values for the C IVλ1549 Range

ObjID	C IVλ1549 BC Flux[a]	λ_{cent}^{b}	Shift[c]	FWHM[c]	EW[b]	C IVλ1549 Blue Flux[a]	λ_{cent}^{b}	Shift[c]	FWHM[c]	EW[b]	C IVλ1549 VBC Flux[a]	λ_{cent}^{b}	Shift[c]	FWHM[c]	EW[b]
206479	129.53 ± 9.55	1548.9 ± 3.6	−22 ± 701	2702 ± 205	27.1 ± 6.5	30.05 ± 2.16	1540.3 ± 5.1	−1689 ± 981	6000 ± 600	6.3 ± 13.9	...	...	...	...	...
206764	235.86 ± 25.03	1549.5 ± 0.2	100 ± 46	2640 ± 114	165.9 ± 3.9	17.35 ± 9.83	1547.0 ± 2.3	−384 ± 445	8000 ± 800	12.4 ± 3.1	36.60 ± 6.56	1557.6 ± 1.1	1662 ± 203	9560 ± 66	27.1 ± 1.0
206427	150.77 ± 9.48	1549.0 ± 0.5	0 ± 97	4412 ± 333	72.9 ± 1.1	20.73 ± 4.17	1538.0 ± 2.9	−2121 ± 554	5901 ± 1176	10.1 ± 0.5	...	...	...	...	...
206623	546.71 ± 14.61	1548.0 ± 1.0	−194 ± 194	4057 ± 258	29.0 ± 0.5	236.36 ± 11.62	1540.8 ± 0.9	−1591 ± 166	7411 ± 284	12.5 ± 0.4	...	...	...	...	...
206433	379.24 ± 6.59	1548.0 ± 1.0	−194 ± 194	3940 ± 141	101.1 ± 1.7	23.53 ± 0.00	1539.0 ± 0.0	−1935 ± 0	5901 ± 389	6.4 ± 0.0	...	...	...	...	...
206672	96.91 ± 15.55	1550.0 ± 1.0	194 ± 194	4986 ± 591	68.9 ± 5.0	15.48 ± 1.98	1522.6 ± 3.2	−5106 ± 616	6243 ± 757	10.6 ± 0.6	51.91 ± 14.20	1580.8 ± 6.6	6154 ± 1280	9771 ± 1870	38.1 ± 4.6
206653	143.26 ± 5.85	1548.0 ± 0.0	−194 ± 0	5056 ± 269	35.8 ± 0.8	...	...	...	...	...	...	...	...	...	...
206510	13.25 ± 0.70	1548.0 ± 1.0	−194 ± 194	2190 ± 175	34.6 ± 0.6	4.44 ± 1.57	1536.0 ± 2.9	−2515 ± 553	6809 ± 714	11.3 ± 1.4	...	...	...	...	...
206473	66.72 ± 4.28	1549.0 ± 0.0	0 ± 0	2986 ± 351	47.1 ± 3.3	...	...	...	...	...	...	...	...	...	...
206475	435.04 ± 17.82	1553.0 ± 0.5	770 ± 93	6472 ± 16	72.9 ± 3.1	27.91 ± 2.41	1524.2 ± 4.1	−4798 ± 802	6819 ± 780	4.6 ± 0.4	123.00 ± 9.78	1589.6 ± 2.2	7847 ± 428	9480 ± 919	20.8 ± 1.7
206666	295.66 ± 9.90	1550.2 ± 0.6	229 ± 114	8410 ± 241	89.7 ± 2.6	10.27 ± 1.18	1506.9 ± 1.3	−8140 ± 248	3424 ± 483	3.1 ± 0.3	57.15 ± 6.36	1596.3 ± 5.8	9156 ± 1125	9407 ± 221	17.5 ± 1.7
206667	115.36 ± 5.09	1547.6 ± 0.3	−271 ± 58	5208 ± 214	164.6 ± 2.1	22.12 ± 3.42	1524.2 ± 1.1	−4797 ± 213	6227 ± 695	29.9 ± 1.4	34.15 ± 3.26	1580.5 ± 2.2	6105 ± 431	8801 ± 649	51.7 ± 1.4
206593	112.86 ± 6.48	1554.5 ± 0.6	1054 ± 108	13671 ± 235	57.4 ± 2.3	...	...	...	...	...	13.43 ± 4.93	1568.0 ± 4.8	3680 ± 924	14184 ± 536	6.9 ± 1.8
206388	106.35 ± 7.62	1550.1 ± 0.8	206 ± 156	3331 ± 178	77.1 ± 5.6	19.98 ± 6.56	1543.3 ± 1.8	−1097 ± 350	6000 ± 600	14.7 ± 4.8	...	...	...	...	...
206512	154.78 ± 5.52	1548.1 ± 0.3	−179 ± 65	6541 ± 304	118.3 ± 2.1	15.57 ± 2.52	1519.8 ± 2.9	−5647 ± 556	7584 ± 1521	11.5 ± 1.0	26.50 ± 2.37	1588.3 ± 1.8	7603 ± 354	8801 ± 739	21.1 ± 0.9
206562	68.41 ± 8.15	1547.9 ± 0.7	−222 ± 140	9814 ± 191	85.3 ± 2.7	...	...	...	...	...	10.03 ± 5.15	1565.6 ± 6.1	3211 ± 1181	10529 ± 631	12.9 ± 1.7
206531	99.57 ± 4.73	1546.6 ± 0.5	−466 ± 89	5446 ± 291	24.1 ± 1.1	6.51 ± 3.36	1522.7 ± 4.6	−5082 ± 882	9170 ± 1530	1.6 ± 0.8	35.96 ± 4.06	1598.3 ± 5.6	9547 ± 1085	12961 ± 1106	9.3 ± 1.0

ObjID	He IIλ1640 BC Flux[a]	λ_{cent}^{b}	Shift[c]	FWHM[c]	EW[b]	He IIλ1640 Blue Flux[a]	λ_{cent}^{b}	Shift[c]	FWHM[c]	EW[b]	He IIλ1640 VBC Flux[a]	λ_{cent}^{b}	Shift[c]	FWHM[c]	EW[b]
206479	...	...	...	...	...	...	...	...	...	...	...	...	...	...	...
206764	...	...	...	...	...	...	...	...	...	...	...	...	...	...	...
206427	5.49 ± 1.64	1640.0	1	4412	3.3 ± 0.2	2.37 ± 1.65	1628.4	−2120	5901	1.4 ± 0.2	...	...	...	...	...
206623	60.49 ± 8.03	1639.0	−270	4057	3.5 ± 0.3	62.69 ± 2.00	1631.3	−1667	7411	3.6 ± 0.1	...	...	...	...	...
206433	72.69 ± 18.38	1639.0	−270	3940	19.3 ± 4.6	2.05 ± 6.17	1629.4	−2011	5901	0.6 ± 1.5	...	...	...	...	...
206672	12.96 ± 3.14	1641.1	117	4986	10.2 ± 1.0	1.62 ± 1.53	1612.1	−5180	6243	1.2 ± 1.1	...	...	...	...	...
206653	27.92 ± 2.59	1639.0	−183	5056	7.6 ± 0.3	...	...	...	...	...	...	...	...	...	...
206510	3.62 ± 0.34	1639.0	−193	2190	10.9 ± 0.3	1.09 ± 0.72	1626.2	−2514	6809	3.2 ± 0.7	...	...	...	...	...
206473	11.11 ± 1.88	1639.5	−96	2986	7.9 ± 1.5	...	...	...	...	...	...	...	...	...	...
206475	86.43 ± 9.71	1644.2	771	6472	14.7 ± 1.7	12.38 ± 9.67	1613.8	−4797	6819	2.1 ± 1.7	58.28 ± 18.04	1682.9	7848	9480	10.0 ± 3.2
206666	37.84 ± 0.91	1641.3	230	8410	11.7 ± 0.2	2.82 ± 0.29	1639.8	−35	1458	0.9 ± 0.1	8.00 ± 2.91	1690.1	9157	9407	2.5 ± 0.8
206667	12.18 ± 0.84	1638.5	−270	5208	20.4 ± 0.4	1.50 ± 0.54	1640.0	6	984	2.5 ± 0.2	7.29 ± 2.18	1673.4	6106	8801	13.0 ± 0.9
206593	24.82 ± 1.12	1645.8	1055	13671	13.2 ± 0.4	1.02 ± 0.35	1643.1	569	893	0.5 ± 0.1	8.20 ± 2.00	1660.1	3681	14184	4.4 ± 0.7
206388	12.90 ± 1.80	1641.1	207	3331	9.4 ± 1.3	2.35 ± 1.13	1634.0	−1097	6000	1.7 ± 0.8	...	...	...	...	...
206512	16.35 ± 1.21	1639.0	−178	6541	13.7 ± 0.5	...	...	...	...	...	4.63 ± 3.17	1681.6	7604	8801	4.0 ± 1.2
206562	4.87 ± 0.71	1638.8	−221	9814	7.2 ± 0.2	...	...	...	...	...	0.48 ± 0.95	1657.6	3212	10529	0.7 ± 0.3
206531	15.00 ± 2.01	1637.5	−466	5446	4.1 ± 0.5	...	...	...	...	...	...	...	...	...	...

ObjID	C IVλ1549 NC Flux[a]	λ_{cent}^{b}	Shift[c]	FWHM[c]	EW[b]	N IV 1486 Flux[a]	λ_{cent}^{b}	Shift[c]	FWHM[c]	EW[b]	O III] 1663 Flux[a]	λ_{cent}^{b}	Shift[c]	FWHM[c]	EW[b]
206479	...	...	...	...	...	...	...	...	...	...	...	...	...	...	...
206764	...	...	...	...	...	14.59 ± 2.01	1486.0 ± 0.7	3 ± 145	2918 ± 481	9.4 ± 0.3	...	...	...	...	...
206427	2.12 ± 2.22	1545.3 ± 0.8	−722 ± 162	530 ± 369	1.1 ± 0.3	15.48 ± 3.50	1486.0 ± 0.5	0 ± 101	5999 ± 1015	6.9 ± 0.4	...	...	...	...	...
206623	0.88 ± 1.95	1548.0 ± 0.0	−194 ± 0	858 ± 334	0.1 ± 0.1	27.96 ± 2.8	1486.0 ± 0.5	0 ± 101	5630 ± 1282	1.4 ± 0.0	50.44 ± 3.84	1663.0 ± 0.0	−87 ± 0	3911 ± 397	3.0 ± 0.1
206433	5.59 ± 2.46	1548.0 ± 0.0	−194 ± 0	875 ± 334	1.5 ± 0.6	...	...	...	...	...	29.91 ± 12.81	1662.1 ± 1.5	−254 ± 274	3916 ± 2217	8.1 ± 3.2
206672	1.58 ± 2.78	1550.7 ± 1.4	337 ± 263	558 ± 531	1.1 ± 0.9	8.08 ± 1.30	1494.6 ± 1.9	1741 ± 383	2259 ± 363	5.4 ± 0.4	4.97 ± 1.59	1666.2 ± 1.1	498 ± 193	1826 ± 736	4.0 ± 0.5
206653	...	...	...	...	...	...	...	...	...	...	12.46 ± 2.05	1663.9 ± 2.7	35896 ± 548	3462 ± 919	3.5 ± 0.3
206510	...	...	...	...	...	...	...	...	...	...	3.35 ± 0.26	1663.0 ± 0.0	0 ± 0	6743 ± 1673	10.5 ± 0.2

Table A3
(Continued)

| | C IV λ1549 BC | | | | | C IV λ1549 Blue | | | | | C IV λ1549 VBC | | | | |
ObjID	Flux[a]	λ_{cent}^{b}	Shift[c]	FWHM[c]	EW[b]	Flux[a]	λ_{cent}^{b}	Shift[c]	FWHM[c]	EW[b]	Flux[a]	λ_{cent}^{b}	Shift[c]	FWHM[c]	EW[b]
206473	⋯	⋯	⋯	⋯	⋯	⋯	⋯	⋯	⋯	⋯	2.53 ± 0.82	1663.5 ± 0.0	90 ± 0	2066 ± 587	1.8 ± 0.6
206475	⋯	⋯	⋯	⋯	⋯	17.66 ± 1.05	1488.9 ± 1.2	594 ± 237	3311 ± 570	2.9 ± 0.2	20.54 ± 5.92	1663.5 ± 0.0	90 ± 0	4021 ± 767	3.5 ± 1.0
206666	14.13 ± 1.60	1548.8 ± 0.4	−36 ± 79	1458 ± 131	4.3 ± 0.4	7.08 ± 0.64	1488.0 ± 0.5	410 ± 106	2173 ± 297	2.1 ± 0.2	8.86 ± 0.40	1663.4 ± 1.4	78 ± 242	3391 ± 261	2.8 ± 0.1
206667	12.24 ± 0.00	1549.0 ± 0.2	5 ± 32	984 ± 50	17.5 ± 0.0	12.88 ± 3.85	1485.0 ± 4.4	−208 ± 878	6293 ± 1609	16.4 ± 1.6	3.81 ± 1.33	1663.7 ± 2.0	124 ± 362	2747 ± 753	6.7 ± 0.6
206593	1.96 ± 0.43	1551.9 ± 0.4	568 ± 80	893 ± 138	1.0 ± 0.2	3.16 ± 0.71	1484.9 ± 1.1	−217 ± 216	5788 ± 1109	1.6 ± 0.3	0.12 ± 0.26	1661.4 ± 3.0	−287 ± 533	3006 ± 2252	0.1 ± 0.1
206388	1.67 ± 1.43	1549.2 ± 1.0	32 ± 193	548 ± 296	1.2 ± 1.1	7.66 ± 0.62	1482.9 ± 3.3	−632 ± 655	5067 ± 862	5.6 ± 0.5	11.84 ± 1.96	1670.4 ± 1.9	1336 ± 334	3792 ± 730	8.7 ± 1.4
206512	0.91 ± 1.18	1549.0 ± 0.0	0 ± 0	646 ± 214	0.7 ± 0.5	14.89 ± 2.04	1487.0 ± 0.6	208 ± 115	6531 ± 728	10.7 ± 0.8	4.30 ± 1.91	1664.7 ± 2.9	310 ± 523	4074 ± 2158	3.7 ± 0.7
206562	4.00 ± 1.03	1548.1 ± 0.4	−169 ± 78	1121 ± 179	5.0 ± 0.4	9.13 ± 0.48	1474.6 ± 3.7	−2309 ± 748	9814 ± 191	9.9 ± 0.2	⋯	⋯	⋯	⋯	⋯
206531	3.89 ± 2.44	1547.0 ± 0.9	−388 ± 181	1138 ± 492	0.9 ± 0.6	⋯	⋯	⋯	⋯	⋯	9.32 ± 3.00	1664.0 ± 4.1	173 ± 740	5446 ± 0	2.6 ± 0.7

Note. *a*, *b*, and *c* indices have the same meanings as those in Table A1.

Table A4
Line Component Values for the 1900 Å Blend

ObjID	C III]λ1909 BC					Si III]λ1892					Al III]λ1860				
	Flux[a]	λ_{cent}[b]	Shift[c]	FWHM[c]	EW[b]	Flux[a]	λ_{cent}[b]	Shift[c]	FWHM[c]	EW[b]	Flux[a]	λ_{cent}[b]	Shift[c]	FWHM[c]	EW[b]
206623	200.51 ± 22.74	1910.0 ± 1.4	152 ± 222	3500 ± 0	14.6 ± 0.8	198.05 ± 27.19	1893.0 ± 1.4	158 ± 214	3608 ± 256	14.2 ± 0.9	78.62 ± 3.45	1859.4 ± 3.8	140 ± 614	3608 ± 256	5.5 ± 0.1
206433	117.65 ± 14.80	1909.0 ± 0.6	0 ± 92	3300 ± 214	23.5 ± 2.4	32.94 ± 9.70	1892.0 ± 2.2	0 ± 350	3300 ± 214	6.5 ± 1.6	5.93 ± 2.19	1858.4 ± 3.8	−19 ± 617	3300 ± 214	1.2 ± 0.4
206653	49.46 ± 2.03	1910.9 ± 0.6	290 ± 96	4701 ± 391	16.9 ± 0.3	20.16 ± 2.82	1890.4 ± 1.7	−259 ± 268	5404 ± 344	6.8 ± 0.4	17.66 ± 0.37	1856.8 ± 5.0	−277 ± 804	5404 ± 344	5.8 ± 0.1
206473	34.29 ± 3.82	1908.0 ± 1.0	−155 ± 158	3499 ± 234	25.2 ± 3.0	15.65 ± 1.85	1893.0 ± 0.3	158 ± 50	3499 ± 234	11.5 ± 1.4	9.83 ± 0.38	1859.4 ± 1.9	140 ± 311	3499 ± 234	7.2 ± 0.3
206475	47.54 ± 4.98	1910.4 ± 3.9	224 ± 611	4330 ± 666	9.3 ± 0.6	24.80 ± 7.99	1893.6 ± 2.6	252 ± 416	4330 ± 666	4.8 ± 0.9	12.73 ± 0.91	1860.0 ± 5.3	234 ± 943	4330 ± 666	2.4 ± 0.1
206666	66.04 ± 0.92	1909.8 ± 0.3	119 ± 39	5556 ± 223	27.9 ± 0.1	25.25 ± 2.64	1893.0 ± 4.1	158 ± 651	7999 ± 942	10.5 ± 0.3	14.78 ± 2.11	1859.4 ± 5.1	140 ± 825	7999 ± 942	5.9 ± 0.2
206667	16.49 ± 0.57	1908.7 ± 1.4	−46 ± 221	3490 ± 872	42.3 ± 0.2	16.55 ± 2.64	1889.0 ± 0.6	−470 ± 102	5652 ± 175	41.3 ± 1.1	7.45 ± 0.24	1855.5 ± 2.0	−489 ± 319	5652 ± 175	17.7 ± 0.1
206593	16.84 ± 7.40	1911.4 ± 3.4	372 ± 534	7494 ± 327	10.7 ± 1.9	12.2 ± 5.3	1893.5 ± 1.1	244 ± 1757	9906 ± 948	7.7 ± 1.4	4.08 ± 0.99	1859.9 ± 1.1	226 ± 176	9906 ± 948	2.5 ± 0.3
206388	31.73 ± 5.13	1908.8 ± 0.8	−36 ± 120	2335 ± 170	23.2 ± 3.8	29.41 ± 3.59	1891.9 ± 0.8	−11 ± 120	2335 ± 170	21.5 ± 2.6	6.91 ± 0.56	1858.0 ± 0.8	−81 ± 122	2335 ± 170	5.0 ± 0.4
206512	26.15 ± 5.07	1908.1 ± 2.3	−138 ± 365	5563 ± 369	29.5 ± 2.0	17.46 ± 4.63	1893.1 ± 2.3	181 ± 362	5563 ± 369	19.4 ± 1.9	6.93 ± 0.41	1859.5 ± 2.3	163 ± 369	5563 ± 369	7.5 ± 0.2
206562	11.09 ± 1.19	1909.9 ± 0.5	137 ± 81	9152 ± 504	22.5 ± 1.3	6.71 ± 0.49	1893.0 ± 3.2	158 ± 501	9152 ± 504	13.5 ± 0.5	2.13 ± 0.33	1859.4 ± 3.2	140 ± 509	9152 ± 504	4.2 ± 0.4
206531	32.21 ± 8.57	1909.7 ± 1.6	105 ± 245	5262 ± 464	12.1 ± 0.7	15.19 ± 12.19	1893.0 ± 1.6	152 ± 247	5262 ± 464	5.6 ± 1.0	12.53 ± 0.41	1859.3 ± 1.6	134 ± 251	5262 ± 464	4.4 ± 0.0
206692	39.15 ± 5.38	1910.0 ± 3.4	155 ± 539	4026 ± 10	15.4 ± 0.5	20.25 ± 0.33	1893.3 ± 3.4	202 ± 543	4026 ± 10	7.8 ± 0.1	12.01 ± 0.45	1859.6 ± 10.6	183 ± 1710	4026 ± 10	4.5 ± 0.0
206482	28.72 ± 12.82	1910.0 ± 1.5	161 ± 237	3710 ± 1357	15.2 ± 4.7	21.51 ± 2.73	1893.3 ± 1.5	209 ± 239	3710 ± 1357	11.3 ± 1.0	9.52 ± 1.74	1859.7 ± 8.2	190 ± 1318	3710 ± 1357	5.0 ± 0.6
206679	6.44 ± 1.38	1909.0 ± 4.2	0 ± 665	5500 ± 277	8.2 ± 4.3	3.96 ± 1.75	1892.3 ± 4.2	47 ± 670	5500 ± 976	5.1 ± 5.5	2.68 ± 0.25	1858.7 ± 4.2	29 ± 682	5500 ± 976	3.5 ± 0.8
206445	33.94 ± 1.20	1909.0 ± 0.5	0 ± 79	5861 ± 334	12.6 ± 0.1	22.75 ± 2.33	1892.3 ± 2.2	47 ± 349	6563 ± 552	8.3 ± 0.3	12.11 ± 0.44	1858.7 ± 2.2	29 ± 355	6563 ± 552	4.3 ± 0.1
206597	23.35 ± 3.52	1909.0 ± 2.9	−2 ± 453	6169 ± 16	17.8 ± 1.4	14.70 ± 4.18	1892.3 ± 2.9	46 ± 458	6169 ± 16	11.1 ± 1.7	4.83 ± 0.45	1858.7 ± 2.9	27 ± 466	6169 ± 16	3.6 ± 0.1
206641	223.66 ± 7.54	1910.0 ± 0.3	156 ± 49	2322 ± 107	10.2 ± 0.1	65.28 ± 3.11	1893.0 ± 0.1	158 ± 21	2322 ± 107	2.9 ± 0.1	16.02 ± 1.69	1859.4 ± 0.1	140 ± 21	2322 ± 107	0.7 ± 0.0

ObjID	C III]λ1909 NC					C III]λ1909 VBC					Fe III				
	Flux	λ_{cent}	Shift	FWHM	EW	Flux	λ_{cent}	Shift	FWHM	EW	Flux				
206623	...	...	...	...	...	...	...	...	...	...	71.97 ± 0.71	± 12.87 0.05	...	...	...
206433	...	...	...	...	...	...	...	...	...	...	45.63 ± 0.54	± 9.7 0.3	...	...	...
206653	1.38 ± 0.64	1910.1 ± 2.3	174 ± 359	997 ± 847	0.5 ± 0.1	...	...	...	...	...	15.70 ± 0.19	± 10.39 0.05	...	...	...
206473	...	...	...	...	...	...	...	...	...	...	5.84 ± 0.04	± 5.00 0.42	...	...	...
206475	3.92 ± 0.00	1909.1 ± 0.8	22 ± 127	1074 ± 267	0.8 ± 0.1	9.34 ± 2.73	1935.8 ± 10.3	4208 ± 1620	10159 ± 1448	1.9 ± 0.3	13.49 ± 0.1349	± 3.44 0.0344	...	...	...
206666	3.85 ± 0.92	1902.0 ± 0.3	−1104 ± 48	625 ± 126	1.6 ± 0.1	5.83 ± 1.15	1938.3 ± 3.4	4603 ± 533	7001 ± 819	2.5 ± 0.1	21.85 ± 0.18	± 11.33 0.06	...	...	...
206667	2.64 ± 2.43	1909.2 ± 0.6	30 ± 89	774 ± 292	6.8 ± 1.0	7.74 ± 2.63	1946.1 ± 1.9	5830 ± 292	11793 ± 130	21.0 ± 1.1	7.64 ± 0.11	± 11.23 0.16	...	...	...
206593	0.11 ± 0.08	1909.4 ± 3.2	62 ± 499	1389 ± 1037	0.1 ± 0.1	5.87 ± 0.96	1950.1 ± 24.3	6460 ± 3812	10484 ± 746	3.8 ± 0.3	5.82 ± 0.10	± 3.81 0.72	...	...	...
206388	1.13 ± 1.55	1909.0 ± 0.5	0 ± 79	546 ± 445	0.8 ± 1.1	...	...	...	...	...	43.43 ± 0.37	± 30.65 0.12	...	...	...
206512	0.71 ± 0.55	1909.0 ± 0.5	0 ± 79	1590 ± 889	0.8 ± 0.2	...	...	...	...	...	11.41 ± 0.46	± 16.47 0.28	...	...	...
206562	0.49 ± 0.15	1907.0 ± 0.9	−314 ± 141	706 ± 221	1.0 ± 0.2	0.35 ± 0.93	1925.4 ± 27.1	2576 ± 4248	8508 ± 2179	0.7 ± 1.0	3.99 ± 0.02	± 4.03 0.51	...	...	...
206531	...	...	...	...	...	5.93 ± 4.99	1928.7 ± 12.7	3088 ± 1992	7200 ± 1257	2.3 ± 0.4	14.15 ± 0.07	± 7.65 0.04	...	...	...
206692	...	...	...	...	...	...	...	...	...	...	18.08 ± 0.06	± 7.43 0.04	...	...	...
206482	...	...	...	...	...	...	...	...	...	...	13.88 ± 0.35	± 7.55 0.91	...	...	...
206679	0.79 ± 0.20	1909.0 ± 0.5	0 ± 79	800 ± 256	1.0 ± 0.6	3.17 ± 0.22	1945.0 ± 3.1	5654 ± 484	9000 ± 936	3.9 ± 0.7	4.08 ± 0.01	± 4.12 0.67	...	...	...
206445	...	...	...	...	...	9.94 ± 1.12	1943.9 ± 0.4	5483 ± 60	7780 ± 463	3.8 ± 0.1	7.64 ± 0.7	± 4.12 0.4	...	...	...
206597	0.54 ± 0.33	1909.0 ± 0.5	0 ± 79	1128 ± 447	0.4 ± 0.1	4.01 ± 1.40	1946.9 ± 16.0	5955 ± 2519	9667 ± 4092	3.1 ± 0.6	13.26 ± 0.13	± 11.99 0.15	...	...	...
206641	10.85 ± 0.87	1908.5 ± 0.9	−79 ± 141	645 ± 80	0.5 ± 0.1	...	...	...	...	...	126.15 ± 0.35	± 9.53 0.02	...	...	...

ObjID	Si IIλ1816					Fe II UV191					N III]λ1750				
	Flux	λ_{cent}	Shift	FWHM	EW	Flux	λ_{cent}	Shift	FWHM	EW	Flux	λ_{cent}	Shift	FWHM	EW
206623	1.40 ± 0.75	1815.0 ± 3.8	−171 ± 628	3608	0.1 ± 0.0	20.62 ± 3.31	1783.1 ± 2.3	−319 ± 383	3608	1.4 ± 0.1	...	...	...	...	...
206433	4.71 ± 1.41	1816.0 ± 3.8	0 ± 632	3300	0.9 ± 0.2	9.41 ± 3.68	1785.0 ± 4.4	0 ± 740	3300	1.8 ± 0.6	...	...	...	...	...
206653	6.72 ± 0.18	1815.0 ± 5.0	−171 ± 824	5404	2.1 ± 0.0	3.81 ± 0.71	1788.7 ± 1.7	621 ± 286	5404	1.2 ± 0.1	...	...	...	...	...
206473	4.56 ± 0.66	1817.0 ± 1.9	171 ± 319	3499	3.3 ± 0.5	2.86 ± 0.91	1786.5 ± 2.5	254 ± 418	3999	2.1 ± 0.7	...	...	...	...	...
206475	8.99 ± 1.53	1817.0 ± 5.9	171 ± 966	4330	1.7 ± 0.2	8.53 ± 1.25	1785.2 ± 3.0	37 ± 508	4330	1.6 ± 0.1	...	...	...	...	...
206666	5.39 ± 2.22	1817.0 ± 5.1	171 ± 846	7999	2.0 ± 0.2	5.37 ± 0.92	1787.1 ± 6.4	357 ± 1067	7999	2.0 ± 0.1	8.35 ± 1.86	1750.0 ± 0.0	0 ± 0	7199 0	2.91 ± 0.19
206667	5.51 ± 0.49	1814.5 ± 2.0	−255 ± 327	5652	12.3 ± 0.2	5.97 ± 0.44	1782.0 ± 2.0	−510 ± 337	5652	12.7 ± 0.2	6.09 ± 0.62	1750.0 ± 0.0	0 ± 0	5087 0	12.26 ± 0.26
206593	2.69 ± 2.78	1819.3 ± 1.1	538 ± 180	9906	1.6 ± 0.7	1.99 ± 2.32	1791.0 ± 2.2	999 ± 370	9906	1.2 ± 0.6	1.35 ± 1.40	1753.3 ± 0.0	558 ± 0	8915 0	0.76 ± 0.36
206388	1.06 ± 0.83	1816.0 ± 0.8	3 ± 125	2335	0.8 ± 0.6	1.84 ± 0.56	1783.7 ± 0.6	−212 ± 106	2335	1.4 ± 0.4	8.39 ± 0.87	1746.4 ± 0.9	−613 ± 146	3018 435	6.17 ± 0.64
206512	1.27 ± 0.46	1816.2 ± 2.3	27 ± 378	5563	1.3 ± 0.2	3.23 ± 0.47	1787.9 ± 1.5	488 ± 244	5563	3.3 ± 0.2	4.43 ± 0.66	1750.3 ± 0.0	48 ± 0	5007 0	4.35 ± 0.26
206562	1.66 ± 0.00	1817.8 ± 3.2	303 ± 509	9152	3.2 ± 0.0	2.37 ± 0.67	1789.6 ± 2.3	764 ± 382	9152	4.5 ± 0.7	2.44 ± 0.65	1751.9 ± 0.0	323 ± 0	8237 0	4.54 ± 0.69
206531	3.19 ± 0.94	1817.6 ± 1.6	271 ± 258	5262	1.1 ± 0.1	2.94 ± 0.62	1789.4 ± 2.2	732 ± 366	5262	1.0 ± 0.1	5.04 ± 0.92	1759.1 ± 1.4	1555 ± 235	3083 631	1.56 ± 0.08

Table A4
(Continued)

	C III]λ1909 BC					Si III]λ1892					Al IIIλ1860				
ObjID	Flux[a]	λ_{cent}^{b}	Shift[c]	FWHM[c]	EW[b]	Flux[a]	λ_{cent}^{b}	Shift[c]	FWHM[c]	EW[b]	Flux[a]	λ_{cent}^{b}	Shift[c]	FWHM[c]	EW[b]
206692	6.56 ± 0.71	1818.3 ± 10.6	376 ± 376	4026	2.3 ± 0.1	3.05 ± 0.99	1788.9 ± 3.7	653 ± 615	2847	1.1 ± 0.1	4.26 ± 5.70	1751.3 ± 1.8	222 ± 308	4107 5059	1.40 ± 0.54
206482	0.91 ± 1.55	1818.4 ± 8.2	400 ± 400	3710	0.5 ± 0.6	2.57 ± 0.99	1788.0 ± 1.5	504 ± 252	3710	1.3 ± 0.4	8.05 ± 3.00	1751.4 ± 3.4	247 ± 588	5189 1782	4.08 ± 1.09
206679	0.99 ± 0.40	1817.0 ± 4.2	166 ± 698	5500	1.4 ± 1.3	1.88 ± 0.38	1788.7 ± 1.9	627 ± 313	5500	2.6 ± 1.2	2.58 ± 0.64	1750.0 ± 0.0	0 ± 0	5500 1725	3.71 ± 2.02
206445	3.73 ± 0.69	1817.0 ± 2.3	166 ± 380	6563	1.3 ± 0.1	0.36 ± 1.58	1788.7 ± 1.9	627 ± 313	6563	0.1 ± 0.2	10.95 ± 3.40	1750.0 ± 0.0	0 ± 0	9720 3161	3.46 ± 0.38
206597	2.46 ± 0.65	1817.0 ± 2.9	164 ± 477	6169	1.8 ± 0.3	3.00 ± 0.78	1788.7 ± 1.9	625 ± 312	6169	2.2 ± 0.3	4.26 ± 0.95	1750.0 ± 0.0	0 ± 0	5887 1168	2.98 ± 0.38
206641	⋯	⋯	⋯	⋯	⋯	⋯	⋯	⋯	⋯	⋯	⋯	⋯	⋯	⋯	⋯

Note. *a*, *b*, and *c* indices have the same meanings as those in Table A1.

Table A5
Line Component Values for the Mg IIλ2800 Region

ObjID	Mg IIλ2800 BC					Mg IIλ2800 VBC					Mg IIλ2800 NC				
	Flux[a]	λ_{cent}^{b}	Shift[c]	FWHM[c]	EW[b]	Flux[a]	λ_{cent}^{b}	Shift[c]	FWHM[c]	EW[b]	Flux[a]	λ_{cent}^{b}	Shift[c]	FWHM[c]	EW[b]
206475	114.28 ± 3.39	2799.9 ± 0.0	0 ± 0	6011 ± 272	38.5 ± 0.3	11.77 ± 0.00	2850.0 ± 0.0	5462 ± 0	13542 ± 747	± 4.1 0.0	⋯	⋯	⋯	⋯	⋯
206666	62.46 ± 3.51	2799.9 ± 0.0	0 ± 0	6000 ± 839	44.6 ± 0.3	⋯	⋯	⋯	⋯	⋯	⋯	⋯	⋯	⋯	⋯
206667	34.29 ± 0.59	2798.9 ± 2.3	−107 ± 249	5500 ± 1459	46.8 ± 0.2	4.08 ± 1.86	2850.0 ± 12.8	5353 ± 1369	8000 ± 1595	± 5.7 0.7	1.36 ± 2.48	2800.0 ± 3.2	0 ± 338	900 ± 682	1.9 ± 1.0
206512	40.84 ± 0.99	2799.2 ± 0.9	−80 ± 101	5598 ± 570	58.0 ± 0.8	9.84 ± 1.38	2867.0 ± 0.0	7283 ± 0	10152 ± 516	± 14.2 1.2	⋯	⋯	⋯	⋯	⋯
206531	42.93 ± 0.78	2804.6 ± 0.0	499 ± 0	3542 ± 157	21.0 ± 0.1	7.40 ± 0.00	2854.3 ± 25.3	5923 ± 2706	11864 ± 699	± 3.7 0.0	1.85 ± 0.00	2804.2 ± 8.8	555 ± 939	1169 ± 1296	0.9 ± 0.0
206692	65.09 ± 2.46	2804.2 ± 0.9	454 ± 101	3899 ± 342	55.6 ± 0.6	⋯	⋯	⋯	⋯	⋯	⋯	⋯	⋯	⋯	⋯
206482	53.26 ± 1.16	2799.5 ± 0.5	−42 ± 49	2758 ± 138	39.2 ± 0.6	⋯	⋯	⋯	⋯	⋯	⋯	⋯	⋯	⋯	⋯
206445	61.71 ± 0.51	2802.5 ± 0.3	275 ± 33	6364 ± 115	44.6 ± 0.1	⋯	⋯	⋯	⋯	⋯	⋯	⋯	⋯	⋯	⋯
206597	29.99 ± 0.38	2798.0 ± 0.9	−209 ± 92	7074 ± 155	30.5 ± 0.3	5.21 ± 0.78	2831.0 ± 9.5	3429 ± 1019	10589 ± 1114	± 5.3 0.6	⋯	⋯	⋯	⋯	⋯
206641	339.17 ± 5.22	2802.0 ± 0.3	222 ± 28	2609 ± 91	22.0 ± 0.1	⋯	⋯	⋯	⋯	⋯	1.26 ± 2.08	2800.0 ± 0.0	107 ± 0	1585 ± 134	0.1 ± 0.1
206557	35.37 ± 0.48	2798.6 ± 0.4	−140 ± 45	4296 ± 99	66.3 ± 0.3	5.34 ± 0.73	2873.9 ± 13.2	8017 ± 1410	11004 ± 440	± 10.3 0.4	⋯	⋯	⋯	⋯	⋯
206570	4.52 ± 0.25	2802.2 ± 2.1	242 ± 223	6098 ± 362	37.9 ± 0.6	0.43 ± 0.41	2831.0 ± 8.4	3429 ± 899	9533 ± 879	± 3.6 1.0	⋯	⋯	⋯	⋯	⋯
206625	35.04 ± 0.90	2797.7 ± 0.7	−235 ± 75	4234 ± 90	60.9 ± 0.8	0.80 ± 0.67	2879.0 ± 13.5	8567 ± 1448	9469 ± 2562	± 1.4 0.6	1.65 ± 0.55	2798.2 ± 0.8	−91 ± 88	1063 ± 255	2.9 ± 0.5
206489	61.68 ± 0.93	2800.4 ± 0.5	50 ± 55	8808 ± 264	67.7 ± 0.3	4.99 ± 0.57	2890.4 ± 10.2	9789 ± 1093	10342 ± 761	± 5.7 0.2	4.61 ± 0.47	2796.1 ± 0.4	−315 ± 43	1611 ± 131	5.1 ± 0.1
206579	94.72 ± 0.76	2800.0 ± 0.0	6 ± 0	3983 ± 73	46.6 ± 0.3	⋯	⋯	⋯	⋯	⋯	4.70 ± 0.45	2799.4 ± 0.4	37 ± 46	600 ± 0	2.3 ± 0.2
206695	7.80 ± 0.22	2801.1 ± 0.4	121 ± 46	1870 ± 121	20.8 ± 0.3	⋯	⋯	⋯	⋯	⋯	⋯	⋯	⋯	⋯	⋯

ObjID	Fe II UV78					Fe II	
	Flux[a]	λ_{cent}^{b}	Shift[c]	FWHM[c]	EW[b]	Flux[a]	
206475	16.16 ± 1.77	2970.0 ± 0.0	578 ± 0	6011 ± 0	5.9 ± 0.1	80.34 ± 5.64	20.5 ± 1.4
206666	5.78 ± 0.00	2850.0 ± 0.0	−11558 ± 0	9500 ± 2128	4.3 ± 0.0	55.94 ± 2.97	29.0 ± 1.5
206667	⋯	⋯	⋯	⋯	⋯	19.69 ± 1.20	28.9 ± 1.8
206512	4.39 ± 1.03	2970.0 ± 0.0	578 ± 0	5598 ± 0	6.4 ± 0.9	38.45 ± 0.84	55.5 ± 1.2
206531	⋯	⋯	⋯	⋯	⋯	32.00 ± 2.76	± 17.3 1.5
206692	5.53 ± 1.40	2965.0 ± 0.0	73 ± 0	3999 ± 132	5.1 ± 0.3	25.26 ± 1.68	10.4 ± 0.7
206482	6.99 ± 1.29	2965.0 ± 0.0	73 ± 0	6312 ± 800	5.3 ± 0.6	23.46 ± 1.51	16.2 ± 1.0
206445	4.02 ± 0.52	2965.0 ± 0.0	73 ± 0	6364 ± 0	2.7 ± 0.1	32.49 ± 3.25	17.5 ± 1.8
206597	2.30 ± 0.39	2965.0 ± 0.0	73 ± 0	7074 ± 0	2.4 ± 0.3	12.78 ± 1.12	11.6 ± 1.0
206641	27.74 ± 21.43	2962.1 ± 11.7	−225 ± 1185	9025 ± 505	1.9 ± 0.5	469.79 ± 24.98	35.5 ± 1.9
206557	3.02 ± 0.41	2965.0 ± 0.0	73 ± 0	4296 ± 0	6.1 ± 0.2	22.90 ± 0.86	36.2 ± 1.4
206625	2.90 ± 0.16	2955.7 ± 3.8	−869 ± 379	6999 ± 871	5.2 ± 0.1	21.08 ± 0.73	24.1 ± 0.8
206489	0.27 ± 0.19	2951.6 ± 3.5	−1281 ± 352	4336 ± 678	0.3 ± 0.1	18.43 ± 1.32	13.3 ± 1.0
206579	10.59 ± 0.00	2949.4 ± 3.8	−1508 ± 388	6522 ± 538	5.3 ± 0.0	78.08 ± 2.18	36.9 ± 1.0
206570	0.75 ± 0.13	2965.0 ± 0.0	73 ± 0	6098 ± 0	6.7 ± 0.3	3.12 ± 0.18	15.2 ± 0.9
206695	⋯	⋯	⋯	⋯	⋯	9.13 ± 0.39	± 25.4 1.1

Note. *a*, *b*, and *c* indices have the same meanings as those in Table A1.

Table A6
Line Component Values for the Hβ Region

ObjID	Hβ BC					Hβ VBC					Hβ NC				
	λ_{cent}^{b}	Shift^c	FWHM^c	EW^b	Flux^a	λ_{cent}^{b}	Shift^c	FWHM^c	EW^b	Flux^a	λ_{cent}^{b}	Shift^c	FWHM^c	EW^b	
206489	49.91 ± 1.41	4861.0 ± 0.0	0 ± 0	10284 ± 112	115.0 ± 0.4	7.39 ± 1.43	4959.9 ± 11.6	6099 ± 713	12131 ± 770	17.5 ± 0.4	...	...	...	...	...
206579	100.91 ± 1.61	4861.0 ± 0.0	0 ± 0	5360 ± 100	125.7 ± 0.7	...	...	...	...	...	6.85 ± 0.50	4862.7 ± 0.3	104 ± 20	444 ± 0	8.5 ± 0.2
206695	9.30 ± 3.24	4861.0 ± 1.6	0 ± 96	3000 ± 637	28.7 ± 10.1	...	...	...	...	...	...	...	...	...	...

ObjID	[O III]λ5007					[O III]λ5007 SB									
206489	10.90 ± 0.16	5007.0 ± 0.2	2 ± 14	711 ± 38	26.1 ± 0.1	...	...	...	...	...	...	...	...	...	...
206579	22.80 ± 0.88	5008.9 ± 0.1	116 ± 5	444 ± 12	29.0 ± 0.4	15.63 ± 0.84	5006.6 ± 0.5	−25 ± 27	1351 ± 105	19.9 ± 0.4	...	...	...	...	...
206695	3.21 ± 0.19	5007.0 ± 0.5	0 ± 27	800 ± 43	10.0 ± 0.6	...	...	...	...	...	...	...	...	...	...

ObjID	He IIλ4687 BC					He IIλ4687 NC					Fe II opt				
206489	7.37 ± 0.64	4686.0 ± 0.0	19 ± 0	10284 ± 0	16.2 ± 0.2	...	...	...	...	...	8.43 ± 0.82	18.4 ± 1.8	...	...	...
206579	17.38 ± 1.02	4686.0 ± 0.0	19 ± 0	5360 ± 0	21.1 ± 0.4	1.15 ± 0.26	4685.7 ± 1.0	−1 ± 66	444 ± 0	1.4 ± 0.1	25.52 ± 1.04	31.4 ± 1.3	...	...	...
206695	...	...	...	...	...	...	...	...	...	...	6.96 ± 0.32	21.7 ± 1.0	...	...	...

ObjID	Hγ BC					Hγ NC					[O III]λ4363				
206489	...	...	...	...	...	...	...	...	...	...	...	...	...	...	...
206579	23.01 ± 0.92	4355.3 ± 1.4	1059 ± 97	5360 ± 0	26.5 ± 0.4	1.95 ± 0.26	4341.6 ± 0.5	112 ± 36	444 ± 0	2.2 ± 0.1	1.71 ± 0.26	4364.5 ± 0.7	101 ± 46	444 ± 0	2.0 ± 0.1
206695	...	...	...	...	...	...	...	...	...	...	...	...	...	...	...

Note. *a, b,* and *c* indices have the same meanings as those in Table A1.

Appendix B
Individual Computations

In this appendix, we report individual computations described in Section 4, of $\log L_{\rm bol}$, $\log M_{\rm BH}$, and $\log R_{\rm Edd}$. The columns in Table B1 are Column (1) Object ID. Columns (2)–(5) are the computations of $\log L_{\rm bol}$ using the corresponding bolometric corrections of Table 2 for each continuum region. Columns (6)–(9) are the computations of $M_{\rm BH}$ using Equation (1) and the α and β values of Table 2 of the corresponding line. Columns (10)–(13) are the $\log R_{\rm Edd}$ for the corresponding $L_{\rm bol}$ and $M_{\rm BH}$.

Table B1
Individual Computations of $\log L_{\rm bol}$, $\log M_{\rm BH}$, and $\log R_{\rm Edd}$

ObjID (1)	$\log L_{\rm bol}^{\rm a}$				$\log M_{\rm BH}^{\rm b}$				$\log R_{\rm Edd}$			
	1450 Å (2)	1700Å (3)	3000 Å (4)	5100 Å (5)	C IV (6)	Al III (7)	Mg II (8)	Hβ (9)	C IV (10)	Al III (11)	Mg II (12)	Hβ (13)
78393	48.00 ± 0.08	⋯	⋯	⋯	9.31 ± 0.31	⋯	⋯	⋯	0.56 ± 0.02	⋯	⋯	⋯
206388	46.23 ± 0.05	46.47 ± 0.02	⋯	⋯	8.61 ± 0.18	8.22 ± 0.17	⋯	⋯	−0.52 ± 0.17	0.15 ± 0.02	⋯	⋯
206427	47.18 ± 0.06	47.46 ± 0.04	⋯	⋯	9.50 ± 0.22	⋯	⋯	⋯	−0.39 ± 0.16	⋯	⋯	⋯
206433	47.23 ± 0.08	47.48 ± 0.01	⋯	⋯	9.40 ± 0.22	9.10 ± 0.11	⋯	⋯	−0.28 ± 0.15	0.28 ± 0.01	⋯	⋯
206445	⋯	46.61 ± 0.01	46.37 ± 0.01	⋯	⋯	9.20 ± 0.10	9.39 ± 0.05	⋯	⋯	−0.68 ± 0.04	−1.10 ± 0.16	⋯
206473	46.22 ± 0.04	46.52 ± 0.02	⋯	⋯	8.52 ± 0.22	8.60 ± 0.13	⋯	⋯	−0.42 ± 0.11	−0.17 ± 0.03	⋯	⋯
206475	46.87 ± 0.04	47.20 ± 0.01	47.12 ± 0.01	⋯	9.61 ± 0.09	9.17 ± 0.20	9.80 ± 0.08	⋯	−0.85 ± 0.28	−0.08 ± 0.02	−0.77 ± 0.08	⋯
206479	47.64 ± 0.07	47.88 ± 0.03	⋯	⋯	9.33 ± 0.24	⋯	⋯	⋯	0.20 ± 0.05	⋯	⋯	⋯
206482	⋯	46.50 ± 0.02	46.49 ± 0.04	⋯	⋯	8.63 ± 0.43	8.73 ± 0.15	⋯	⋯	−0.24 ± 0.03	−0.35 ± 0.10	⋯
206489	⋯	⋯	45.58 ± 0.01	45.80 ± 0.03	⋯	⋯	9.18 ± 0.05	9.33 ± 0.09	⋯	⋯	−1.70 ± 0.43	−1.70 ± 1.74
206510	46.12 ± 0.08	46.23 ± 0.05	⋯	⋯	8.25 ± 0.26	⋯	⋯	⋯	−0.15 ± 0.11	⋯	⋯	⋯
206512	46.20 ± 0.04	46.38 ± 0.02	46.36 ± 0.04	⋯	9.21 ± 0.13	8.92 ± 0.13	9.27 ± 0.19	⋯	−1.10 ± 0.49	−0.64 ± 0.06	−1.00 ± 0.39	⋯
206531	46.43 ± 0.03	46.77 ± 0.01	46.67 ± 0.07	⋯	9.21 ± 0.12	9.09 ± 0.12	9.06 ± 0.20	⋯	−0.85 ± 0.22	−0.43 ± 0.02	−0.49 ± 0.22	⋯
206557	⋯	⋯	45.67 ± 0.04	⋯	⋯	⋯	8.61 ± 0.11	⋯	⋯	⋯	⋯	⋯
206562	46.05 ± 0.06	46.09 ± 0.02	⋯	⋯	9.45 ± 0.16	9.18 ± 0.13	⋯	⋯	−1.52 ± 2.03	−1.22 ± 0.29	⋯	⋯
206570	⋯	⋯	44.85 ± 0.04	⋯	⋯	⋯	8.40 ± 0.15	⋯	⋯	⋯	−1.70 ± 1.95	⋯
206579	⋯	⋯	45.69 ± 0.02	45.77 ± 0.01	⋯	⋯	8.56 ± 0.05	8.75 ± 0.04	⋯	⋯	−0.96 ± 0.12	−1.10 ± 0.11
206593	46.46 ± 0.05	46.70 ± 0.01	⋯	⋯	10.00 ± 0.14	9.60 ± 0.06	⋯	⋯	−1.70 ± 2.61	−1.00 ± 0.09	⋯	⋯
206597	⋯	⋯	46.17 ± 0.01	⋯	⋯	⋯	9.35 ± 0.05	⋯	⋯	⋯	−1.30 ± 0.26	⋯
206623	47.70 ± 0.01	47.95 ± 0.01	⋯	⋯	9.74 ± 0.10	9.45 ± 0.12	⋯	⋯	−0.12 ± 0.02	0.40 ± 0.00	⋯	⋯
206625	⋯	⋯	45.54 ± 0.02	⋯	⋯	⋯	8.52 ± 0.06	⋯	⋯	⋯	−1.10 ± 0.22	⋯
206641	⋯	⋯	47.30 ± 0.01	⋯	⋯	⋯	9.18 ± 0.06	⋯	⋯	⋯	0.01 ± 0.01	⋯
206653	47.05 ± 0.03	47.34 ± 0.01	⋯	⋯	9.52 ± 0.12	9.45 ± 0.11	⋯	⋯	−0.55 ± 0.09	−0.21 ± 0.01	⋯	⋯
206666	46.69 ± 0.02	46.95 ± 0.01	⋯	⋯	9.73 ± 0.07	9.56 ± 0.06	⋯	⋯	−1.15 ± 0.25	−0.72 ± 0.05	⋯	⋯
206667	46.08 ± 0.04	46.17 ± 0.02	46.41 ± 0.05	⋯	8.96 ± 0.14	8.81 ± 0.25	9.28 ± 0.39	⋯	−0.92 ± 0.36	−0.74 ± 0.14	−0.96 ± 0.47	⋯
206672	46.74 ± 0.03	46.94 ± 0.02	⋯	⋯	9.32 ± 0.18	⋯	⋯	⋯	−0.66 ± 0.12	⋯	⋯	⋯
206679	⋯	45.98 ± 0.03	⋯	⋯	⋯	8.68 ± 0.16	⋯	⋯	⋯	−0.80 ± 0.16	⋯	⋯
206692	⋯	46.71 ± 0.01	46.38 ± 0.11	⋯	⋯	8.83 ± 0.03	8.97 ± 0.33	⋯	⋯	−0.22 ± 0.01	−0.68 ± 0.50	⋯
206695	⋯	⋯	44.67 ± 0.02	45.13 ± 0.02	⋯	⋯	7.27 ± 0.10	7.92 ± 0.27	⋯	⋯	−0.70 ± 0.09	−0.89 ± 0.17
206764	47.16 ± 0.12	⋯	⋯	⋯	9.06 ± 0.33	⋯	⋯	⋯	0.07 ± 0.11	⋯	⋯	⋯

Notes.
a Units are erg per second.
b Units are in solar mass.

ORCID iDs

Castalia Alenka Negrete ● https://orcid.org/0000-0002-1656-827X
Héctor J. Ibarra-Medel ● https://orcid.org/0000-0002-9790-6313
Erika Benítez ● https://orcid.org/0000-0003-1018-2613
Irene Cruz-González ● https://orcid.org/0000-0002-2653-1120
Yair Krongold ● https://orcid.org/0000-0001-6291-5239
J. Jesús González ● https://orcid.org/0000-0002-3724-1583
Jordi Cepa ● https://orcid.org/0000-0002-6566-724X
Martín Herrera-Endoqui ● https://orcid.org/0000-0002-8653-020X
Takamitsu Miyaji ● https://orcid.org/0000-0002-7562-485X
J. Antonio de Diego ● https://orcid.org/0000-0001-7040-069X

References

Abdurro'uf, Accetta, K., Aerts, C., et al. 2022, ApJS, 259, 35
Bachev, R., Marziani, P., Sulentic, J. W., et al. 2004, ApJ, 617, 171
Baldwin, J. A. 1977, ApJ, 214, 679
Baldwin, J. A., Phillips, M. M., & Terlevich, R. 1981, PASP, 93, 5
Benítez, E., Jiménez-Bailón, E., Negrete, C. A., et al. 2022, MNRAS, 516, 5270
Benítez, E., Ibarra-Medel, H., Negrete, C. A., et al. 2023, ApJ, 952, 45
Bian, W.-H., Fang, L.-L., Huang, K.-L., & Wang, J.-M. 2012, MNRAS, 427, 2881
Boquien, M., Burgarella, D., Roehlly, Y., et al. 2019, A&A, 622, A103
Boroson, T. A., & Green, R. F. 1992, ApJS, 80, 109
Bruhweiler, F., & Verner, E. 2008, ApJ, 675, 83
Buendia-Rios, T. M., Negrete, C. A., Marziani, P., & Dultzin, D. 2023, A&A, 669, A135
Buendia–Rios, T. M., Marziani, P., Negrete, C. A., & Dultzin, D. 2025, MNRAS, 540, 562
Cardelli, J. A., Clayton, G. C., & Mathis, J. S. 1989, ApJ, 345, 245
Dickey, J. M., & Lockman, F. J. 1990, ARA&A, 28, 215
Elvis, M. 2000, ApJ, 545, 63
Ferland, G. J., Hu, C., Wang, J., et al. 2009, ApJL, 707, L82
Fotopoulou, S., Salvato, M., Hasinger, G., et al. 2012, ApJS, 198, 1
Francis, P. J., Hewett, P. C., Foltz, C. B., et al. 1991, ApJ, 373, 465
Garnica, K., Negrete, C. A., Marziani, P., et al. 2022, A&A, 667, A105
Ge, X., Bian, W.-H., Jiang, X.-L., Liu, W.-S., & Wang, X.-F. 2016, MNRAS, 462, 966
Gonzalez-Otero, M., Padilla-Torres, C. P., Cepa, J., et al. 2023, A&A, 669, A85
González-Otero, M., Cepa, J., Padilla-Torres, C. P., et al. 2024, A&A, 687, A19
Grünwald, G., Boller, T., Rakshit, S., et al. 2023, A&A, 669, A37
Ibarra-Medel, H., Negrete, C. A., Lacerna, I., et al. 2025, MNRAS, 536, 752
Jenaro-Ballesteros, N. 2023, BSc thesis, Universidad Nacional Autónoma de México Ciudad de México http://132.248.9.195/ptd2023/octubre/0847307/Index.html
Jordi, K., Grebel, E. K., & Ammon, K. 2006, A&A, 460, 339
Juarez, Y., Maiolino, R., Mujica, R., et al. 2009, A&A, 494, L25
Kollatschny, W., & Zetzl, M. 2013, A&A, 549, A100
Kondapally, R., Best, P. N., Hardcastle, M. J., et al. 2021, A&A, 648, A3
Kovačević, J., Popović, L. Č., & Dimitrijević, M. S. 2010, ApJS, 189, 15
Krawczyk, C. M., Richards, G. T., Mehta, S. S., et al. 2013, ApJS, 206, 4
Kriss, G. 1994, in ASP Conf. Ser. 61, Astronomical Data Analysis Software and Systems III, ed. D. R. Crabtree, R. J. Hanisch, & J. Barnes (San Francisco, CA: ASP), 437
Lehmann, I., Hasinger, G., Schmidt, M., et al. 2000, A&A, 354, 35
Lockman, F. J., Jahoda, K., & McCammon, D. 1986, ApJ, 302, 432
Loiacono, F., Decarli, R., Mignoli, M., et al. 2024, A&A, 685, A121
Lutz, D., Poglitsch, A., Altieri, B., et al. 2011, A&A, 532, A90
Martínez-Aldama, M. L., Del Olmo, A., Marziani, P., et al. 2018, FrASS, 4, 65
Marziani, P., & Sulentic, J. W. 2014, MNRAS, 442, 1211
Marziani, P., Sulentic, J. W., Negrete, C. A., et al. 2010, MNRAS, 409, 1033
Marziani, P., Dultzin, D., Sulentic, J. W., et al. 2018, FrASS, 5, 6
Marziani, P., del Olmo, A., Martínez-Carballo, M. A., et al. 2019, A&A, 627, A88
Marziani, P., Bon, E., Bon, N., et al. 2022, AN, 343, e210082
Marziani, P., Sulentic, J. W., Plauchu-Frayn, I., & del Olmo, A. 2013a, ApJ, 764, 150
Marziani, P., Sulentic, J. W., Plauchu-Frayn, I., & del Olmo, A. 2013b, A&A, 555, A89
Marziani, P., Sulentic, J. W., Zwitter, T., Dultzin-Hacyan, D., & Calvani, M. 2001, ApJ, 558, 553
Marziani, P., Sulentic, J. W., Stirpe, G. M., Zamfir, S., & Calvani, M. 2009, A&A, 495, 83
Mengistue, S. T., Del Olmo, A., Marziani, P., et al. 2023, MNRAS, 525, 4474
Negrete, C. A., Dultzin, D., Marziani, P., et al. 2018, A&A, 620, A118
Negrete, C. A., Dultzin, D., Marziani, P., & Sulentic, J. W. 2012, ApJ, 757, 62
Negrete, C. A., Dultzin, D., Marziani, P., & Sulentic, J. W. 2013, ApJ, 771, 31
Negrete, C. A., Dultzin, D., Marziani, P., & Sulentic, J. W. 2014, ApJ, 794, 95
Osterbrock, D. E. 1981, ApJ, 249, 462
Panda, S. 2024, FrASS, 11, 1479874
Panda, S., Martínez-Aldama, M. L., & Zajaček, M. 2019, FrASS, 6, 75
Press, W. H., Flannery, B. P., & Teukolsky, S. A. 1986, Numerical Recipes. The Art of Scientific Computing (Cambridge: Cambridge Univ. Press)
Prince, R., Zajaček, M., Panda, S., et al. 2023, A&A, 678, A189
Proga, D., Stone, J. M., & Kallman, T. R. 2000, ApJ, 543, 686
Rauch, M. 1998, ARA&A, 36, 267
Richards, G. T., Strauss, M. A., Fan, X., et al. 2006, AJ, 131, 2766
Richards, G. T., Kruczek, N. E., Gallagher, S. C., et al. 2011, AJ, 141, 167
Rovilos, E., Fotopoulou, S., Salvato, M., et al. 2011, A&A, 529, A135
Sameshima, H., Maza, J., Matsuoka, Y., et al. 2009, MNRAS, 395, 1087
Schneider, D. P., Schmidt, M., Hasinger, G., et al. 1998, AJ, 115, 1230
Shen, Y., & Ho, L. C. 2014, Natur, 513, 210
Shin, J., Woo, J.-H., Nagao, T., Kim, M., & Bahk, H. 2021, ApJ, 917, 107
Sulentic, J. W., Marziani, P., & Dultzin-Hacyan, D. 2000a, ARA&A, 38, 521
Sulentic, J. W., Marziani, P., del Olmo, A., et al. 2014, A&A, 570, A96
Sulentic, J. W., del Olmo, A., Marziani, P., et al. 2017, A&A, 608, A122
Sulentic, J. W., Zwitter, T., Marziani, P., & Dultzin-Hacyan, D. 2000b, ApJL, 536, L5
Sulentic, J. W., Bachev, R., Marziani, P., Negrete, C. A., & Dultzin, D. 2007, ApJ, 666, 757
Trakhtenbrot, B., & Netzer, H. 2012, MNRAS, 427, 3081
Vanden Berk, D. E., Richards, G. T., Bauer, A., et al. 2001, AJ, 122, 549
Vestergaard, M., & Wilkes, B. J. 2001, ApJS, 134, 1
Vestergaard, M., & Peterson, B. M. 2006, ApJ, 641, 689
Wang, Y., Liu, W., Shang, Z., & Brotherton, M. S. 2022, MNRAS, 515, 5836
Wisotzki, L., Christlieb, N., Bade, N., et al. 2000, A&A, 358, 77
Wu, Q., & Shen, Y. 2022, ApJS, 263, 42
Zamanov, R., Marziani, P., Sulentic, J. W., et al. 2002, ApJL, 576, L9
Zamfir, S., Sulentic, J. W., Marziani, P., & Dultzin, D. 2010, MNRAS, 403, 1759
Zheng, W., & Malkan, M. A. 1993, ApJ, 415, 517